

Effect of primordial non-Gaussianities on the far-UV luminosity function of high-redshift galaxies: implications for cosmic reionization

Jacopo Chevallard^{1*}, Joseph Silk^{1,2}, Takahiro Nishimichi¹, Melanie Habouzit¹, Gary A. Mamon¹, Sébastien Peirani¹

¹*UPMC-CNRS, UMR7095, Institut d'Astrophysique de Paris, F-75014, Paris, France*

²*Department of Physics and Astronomy, The Johns Hopkins University, Baltimore MD 20218, USA*

Submitted to MNRAS on

ABSTRACT

Understanding how the intergalactic medium (IGM) was reionized at $z \gtrsim 6$ is one of the big challenges of current high redshift astronomy. It requires modelling the collapse of the first astrophysical objects (Pop III stars, first galaxies) and their interaction with the IGM, while at the same time pushing current observational facilities to their limits. The observational and theoretical progress of the last few years have led to the emergence of a coherent picture in which the budget of hydrogen-ionizing photons is dominated by low-mass star-forming galaxies, with little contribution from Pop III stars and quasars. The reionization history of the Universe therefore critically depends on the number density of low-mass galaxies at high redshift. In this work, we explore how changes in the cosmological model, and in particular in the statistical properties of initial density fluctuations, affect the formation of early galaxies. Following Habouzit et al. (2014), we run 5 different N-body simulations with Gaussian and (scale-dependent) non-Gaussian initial conditions, all consistent with *Planck* constraints. By appealing to a phenomenological galaxy formation model and to a population synthesis code, we compute the far-UV galaxy luminosity function down to $M_{\text{FUV}} = -14$ at redshift $7 \leq z \leq 15$. We find that models with strong primordial non-Gaussianities on \lesssim Mpc scales show a far-UV luminosity function significantly enhanced (up to a factor of 3 at $z = 14$) in low-mass galaxies. We adopt a reionization model calibrated from state-of-the-art hydrodynamical simulations and show that such scale-dependent non-Gaussianities leave a clear imprint on the Universe reionization history and electron Thomson scattering optical depth τ_e . Although current uncertainties in the physics of reionization and on the determination of τ_e still dominate the signatures of non-Gaussianities, our results suggest that τ_e could ultimately be used to constrain the statistical properties of initial density fluctuations.

Key words:

1 INTRODUCTION

Most baryons in the Universe exist in the form of ionized gas (mainly hydrogen and helium) in the intergalactic medium (IGM) (e.g. Fukugita et al. 1998; Cen & Ostriker 2006). The IGM plays the role of a gas reservoir by feeding dark-matter haloes with fresh gas available for star formation, in this way connecting the properties of large-scale structures to those of single haloes and galaxies. At very early times ($z \gtrsim 20$), gas in the IGM is neutral, and it remains neutral until the appearance of the first sources of ionizing radiation, namely metal-free Pop III stars, early galaxies and

quasars. These sources can potentially provide enough photons to almost fully ionize the IGM by redshift ~ 6 (e.g. Fan et al. 2006).

Although the details of Universe ‘reionization’ are still uncertain, the last decade has seen an impressive improvement of our knowledge of this phase thanks to large observational and modelling efforts. On the one hand, very deep multi-wavelength images have allowed the detection of $\gtrsim 1500$ galaxy candidates at (photometric) redshift $z > 6$ (e.g. Oesch et al. 2013; Bouwens et al. 2014). This has allowed the first statistical studies of galaxy populations at high redshift, e.g. the accurate determination of the ultraviolet galaxy luminosity function up to $z = 8$ (Bouwens et al. 2014). On the other hand, state-of-the-art hydrodynamic simulations are exploring, with improved resolution and refined phys-

* e-mail: chevalla@iap.fr

ical recipes, the formation of the first galaxies and their contribution to the reionization process (e.g. So et al. 2014; Wise et al. 2014). At present, there is broad agreement on Universe reionization being driven by UV radiation emitted by hot, massive stars born in the first galaxies. The low number density of quasars at high redshift ($z \gtrsim 6$) make their contribution to reionization negligible (e.g. Hopkins et al. 2007; Faucher-Giguère et al. 2009), while many computations have shown that the contribution from metal-free, population III stars is also of secondary importance (e.g. Paardekooper et al. 2013; Wise et al. 2014). This means that a crucial ingredient for any reionization model is the number of ionizing photons emitted by early galaxies. This number depends, among other factors, on the number density of galaxies emitting UV radiation at different redshifts, that is on the evolution with time of the far-UV galaxy luminosity function. Several works so far have explored the effect on cosmic reionization of assumptions about the far-UV luminosity function of galaxies, such as the minimum mass of a halo able to sustain star formation and the shape of the faint-end of the luminosity function, assuming a fixed cosmological model.

In this work, we adopt a different approach, exploring the effect of varying the cosmological model, and in particular the statistical properties of initial density perturbations. These perturbations, usually described by a Gaussian random field, evolve with time causing the collapse of dark matter particles, and at later times of baryons, into haloes. The assumption of Gaussian initial density perturbations is supported, at large scales, by the measurements of the temperature fluctuation of the cosmic microwave background (CMB) radiation. In particular, the recent analysis by the *Planck* satellite puts a stringent constraint on the magnitude of a possible departure from Gaussianity using multipoles $\ell < 2500$, which corresponds to $k \lesssim 0.18 \text{ Mpc}^{-1}$ in comoving wave number (Planck Collaboration et al. 2013).

There is still, however, room for significant non-Gaussianities on smaller scales beyond the reach of CMB observations. Some inflationary models indeed predict the presence of scale-dependent non-Gaussian initial density perturbations (e.g., Dirac-Born-Infeld inflation: Silverstein & Tong 2004; Alishahiha et al. 2004; Chen 2005). It is possible for these models to pass the CMB constraints, while leaving a significant impact on structure formation relevant to fluctuations on smaller scales. Although previous theoretical work has shown that the scale-dependence of non-Gaussianities can alter the abundance and clustering of collapsed objects, these studies mainly focus on the high-mass end of the mass function and at late times (Lo Verde et al. 2008; Shandera et al. 2011; Becker et al. 2011), with the exception of the work by Crociani et al. (2009), which focused on the reionization epoch. Given the already tight constraints on primordial non-Gaussianities on large scales, their imprint on smaller objects that formed at an earlier stage would be a complementary probe for understanding the statistical properties of the initial cosmic perturbations over a wider dynamic range.

Habouzit et al. (2014, hereafter paper I) have recently considered the effects of scale-dependent non-Gaussianity on the halo and stellar mass functions of galaxies. For this, four cosmological N-body simulations were run, each with different spectra for the scale-dependence of the local non-Gaussianity, plus an additional one with Gaussian initial conditions, all with the same phases. The level of non-Gaussianity was high on Galactic scales, but low enough to be consistent with the CMB constraints from the *Planck* mission on cluster scales and larger. A simple galaxy formation model was applied to the halo merger trees run forward in time: this was based on the redshift-dependent stellar to halo mass rela-

tion of Behroozi et al. (2013), which was modified to prevent stellar masses from decreasing in time. Paper I concludes that the stellar mass function is significantly altered if the non-Gaussianity varies very strongly with scale.

In the present work, we analyse the same cosmological simulations as in paper I, extending the analysis of paper I in several ways. We appeal to the simple, physically motivated, galaxy formation model of Mutch et al. (2013) to compute the stellar mass assembly in each dark matter halo. Next, we adopt the Bruzual & Charlot (2003) stellar population synthesis code to compute the far-UV luminosity function of galaxies in the redshift range $7 \leq z \leq 15$. Finally, we consider a ‘standard’ reionization model and compute the reionization history of the Universe, exploring the impact of the different scale-dependent non-Gaussianities on reionization.

In Section 2 below, we describe the cosmological simulations along with the algorithms used to generate the non-Gaussian initial conditions, to identify haloes and build merger trees. We also present the simple galaxy formation model of Mutch et al. (2013), as well as our additions to and modifications of the model. In Section 3, we show the effect of different scale-dependent non-Gaussianities on the halo and stellar mass functions, and on the far-UV luminosity function of galaxies at redshift $7 \leq z \leq 15$. In Section 4, we present the reionization model that we later adopt to compute the reionization history of the Universe. In Section 5, we quantify the impact of different levels of non-Gaussian initial density perturbations on the Universe reionization history and on the optical depth of electrons to Thomson scattering. In Section 6, we discuss the assumptions of our reionization model and the possible sources of uncertainty. Finally, we discuss in Section 7 the implications of our findings on Universe reionization, and we highlight how more accurate measurements of the electron Thomson scattering optical depth can be used to constrain the level of primordial non-Gaussianities.

2 MODEL

We start by presenting the simulation setup, i.e. the algorithm we used to generate the (Gaussian and non-Gaussian) initial density perturbations and the N-body code adopted to compute their time evolution. We also introduce the codes we employ to identify the dark matter haloes at each time-step of the simulations and to build the merger trees. We end this section by introducing the analytic galaxy formation model of Mutch et al. (2013), along with our modification on the efficiency of baryon conversion into stars and addition of a prescription for the chemical evolution of galaxies, and the Bruzual & Charlot (2003) population synthesis code.

2.1 Non-Gaussian initial density perturbations

The statistical properties of the initial density perturbations depend on the high energy physics adopted at the very first instants of the Universe. Assuming the inflationary paradigm, this means that these density perturbations are linked to the details of the adopted inflationary model. The simplest model of inflation, a single slowly-rolling scalar field, predicts nearly Gaussian initial density perturbations, while more complicated models lead to non-Gaussianities of different shapes, amplitudes and scale-dependences.

If the initial density perturbations are purely Gaussian, the density field can be fully described by the two-point correlation

function (i.e. the power spectrum in Fourier space), since all higher order moments are zero. The three-point correlation function (i.e. the ‘bispectrum’ in Fourier space) is the lowest order statistic affected by the presence of non-Gaussianities. It can be measured by considering triangles in the Fourier space, and the shape of the triangles, i.e. the relative magnitude of the wave vectors, is linked to the physical mechanism creating such non-Gaussianities.

In this work, we consider non-Gaussianities of ‘local’ type, corresponding to ‘squeezed’ triangles in which two wave vectors have similar magnitudes and are much larger than the third one ($k_1 \simeq k_2 \gg k_3$). This type of primordial non-Gaussianity originates from inflationary models whose non-linearities develop on super-horizon scales (e.g. ‘curvaton’ models, multi-field inflation, see Yadav & Wandelt 2010).

To compute the impact of primordial non-Gaussianities on early structure formation, we firstly generate the non-Gaussian initial conditions at $z = 200$ using a parallel non-Gaussian code developed and updated in Nishimichi et al. (2009); Valageas & Nishimichi (2011); Nishimichi (2012). This code is based on second-order Lagrangian perturbation theory (e.g., Scoccimarro 1998; Crocce et al. 2006) with pre-initial particles placed on a regular lattice. We consider the phenomenological model for scale-dependent non-Gaussianities of Becker et al. (2011) (i.e. *generalized local ansatz*)

$$\zeta(\mathbf{x}) = \zeta_G(\mathbf{x}) + \frac{3}{5} [f_{\text{NL}} * (\zeta_G^2 - \langle \zeta_G^2 \rangle)](\mathbf{x}), \quad (1)$$

where ζ denotes the curvature perturbation, ζ_G a Gaussian random field and f_{NL} the scale-dependent amplitude of non-Gaussianity. The convolution is defined in Fourier space as a multiplication by a scale-dependent coefficient

$$f_{\text{NL}}(k) = f_{\text{NL}}^0 \left(\frac{k}{k_0} \right)^\gamma, \quad (2)$$

where f_{NL}^0 indicates the magnitude of non-Gaussianity at the scale $k = k_0$.

This model is a generalization of the so-called local-type non-Gaussianity (Komatsu & Spergel 2001). It has two parameters, f_{NL}^0 and γ , that determine the amplitude and the slope of the function $f_{\text{NL}}(k)$, respectively. We recover the (scale-independent) local non-Gaussianity by setting $\gamma = 0$. The parameters of the models used in this work are taken from paper I, listed in Table 1 and plotted in Fig. 1. We also show in Fig. 1 the constraint on $f_{\text{NL}}(k)$ by Planck Collaboration et al. (2013) as a gray shaded region. We consider models with $\gamma > 0$ such that the magnitude of non-Gaussianity is large on galactic scales, while being below the observational upper limit on the scales probed by *Planck* observations. Also, the sign convention for f_{NL} is chosen such that a positive f_{NL} leads to a positive skewness in the initial matter fluctuations.

2.2 Dark matter simulations

Previous studies have shown, analytically and by means of N-body simulations, the effect of scale-invariant primordial non-Gaussianities on the halo mass function and halo power spectrum (Nishimichi et al. 2010; Nishimichi 2012). In this work, we appeal to the N-body simulations presented in paper I, which we briefly summarize below, to study how scale-dependent initial non-Gaussianities affect structure formation at redshift $7 \leq z \leq 15$.

Simulation	f_{NL}^0	γ	Haloos at $z = 6.5$
Gaussian	-	-	331 139
non-Gaussian 1	82	1/2	324 181
non-Gaussian 2	10^3	4/3	337 388
non-Gaussian 3	7.357×10^3	2	374 653
non-Gaussian 4	10^4	4/3	491 577

Table 1. Parameters defining the non-Gaussian term in the initial density perturbations (see Equation 2) at the pivot wave number $k_0 = 100 h \text{Mpc}^{-1}$, and number of haloos (excluding satellites) identified by ADAPTAHOP at the final step of our simulations ($z = 6.5$).

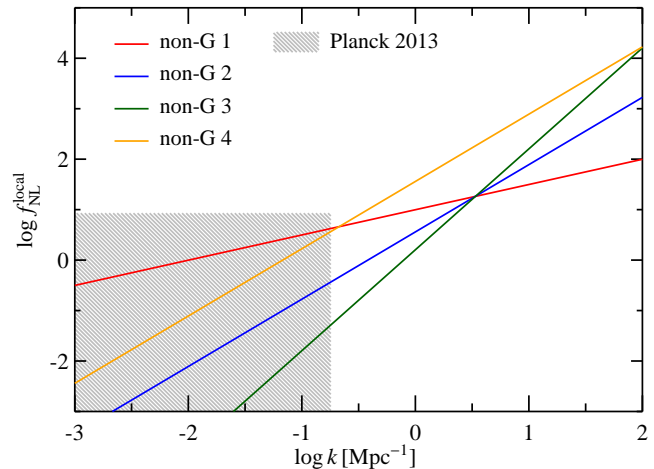


Figure 1. Level of non-Gaussianity of local type at different scales for the different models adopted in this work, parametrized with a power law as in Equation 2. The red line indicates the non-Gaussian model 1 ($f_{\text{NL}}^0 = 82$ and $\gamma = 1/2$); blue the non-Gaussian model 2 ($f_{\text{NL}}^0 = 10^3$ and $\gamma = 4/3$); dark-green the non-Gaussian model 3 ($f_{\text{NL}}^0 = 7357$ and $\gamma = 2$) and orange the non-Gaussian model 4 ($f_{\text{NL}}^0 = 10^4$ and $\gamma = 4/3$). The hatched region shows the allowed region of f_{NL}^0 at scales $k \lesssim 0.18 \text{Mpc}^{-1}$ (68 % credible interval) from Planck Collaboration et al. (2013).

We adopt the smoothed particle hydrodynamics code GADGET2 (Springel et al. 2001; Springel 2005) to run the N-body simulations. We fix the cosmological parameters to the values obtained by the *Planck* mission ‘*Planck*+WP+highL+BAO’ in Table 5 of Planck Collaboration 2014), namely $\Omega_\Lambda = 0.693$, $\Omega_m = 0.307$, $h = 0.678$ and $\sigma_8 = 0.829$. We perform all the simulations in a periodic box of side $50 h^{-1} \text{Mpc}$ with 1024^3 particles; the mass of each dark matter particle is therefore $\sim 9.9 \times 10^6 h^{-1} M_\odot$.

We run a set of 5 different N-body simulations, starting each simulations at $z = 200$ and evolving it till $z = 6.5$, taking snapshots every $\sim 40 \text{Myr}$. We identify dark matter haloos and sub-haloos by means of ADAPTAHOP (Aubert et al. 2004), a (sub)structure finder based on the identification of saddle points in the (smoothed) density field, fixing the density threshold $\delta\rho/\rho_c = 180$, where ρ_c is the critical density of the Universe. We consider only haloos containing > 20 particles ($M_{\text{halo}} \gtrsim 2.9 \times 10^8 M_\odot$) and build the merger trees by means of TREEMAKER (Tweed et al. 2009).

2.3 The Mutch et al. (2013) galaxy formation model

Many approaches have been adopted to describe the assembly of stellar mass in dark-matter haloes. Semi-analytic models (e.g. Kauffmann et al. 1993; Cole et al. 2000; Croton et al. 2006; Lu et al. 2011) are multi-parameters models which adopt analytic relations to describe the baryonic processes (e.g. gas accretion, galaxy interactions, stellar and AGN feedback) that regulate star formation and chemical enrichment in galaxies. Halo occupation distribution models (HOD) are defined in terms of the statistical properties of dark-matter haloes, i.e. of the probability of a halo of given mass to host a given number of galaxies, without any explicit connection to the physical processes acting in galaxies (e.g. Berlind & Weinberg 2002; Berlind et al. 2003; Zheng et al. 2005). Halo abundance matching (HAM) is another statistical approach in which the cumulative mass functions of haloes and galaxies are matched under the assumption of a monotonic relation between stellar and halo masses (i.e. more massive haloes contains more massive galaxies) (e.g. Conroy et al. 2006; Moster et al. 2013).

In spite of the variety of these approaches, they all suffer from limitations which do not make them suitable for our purposes. Semi-analytic models suffer from the presence of many adjustable parameters (usually $\gtrsim 10$) that can be partially constrained by observations in the local Universe (e.g. Lu et al. 2011; Henriques et al. 2013), but remain largely unconstrained at higher redshift. Statistical approaches such as HOD and HAM consider only the average properties of haloes of given mass, therefore not accounting for the stochasticity that is inherent to the hierarchical growth of dark matter haloes.

These reasons have motivated over the last years the emergence of another kind of galaxy formation model in which the complexity of the baryonic physics is subsumed and simplified into a few analytic functions (e.g. Tacchella et al. 2013; Behroozi et al. 2013; Mutch et al. 2013). The advantage of these phenomenological models is that they do not suffer from the presence of multiple, unconstrained parameters typical of semi-analytic models, while allowing one to link the evolution of stellar mass in dark matter haloes to physical quantities, and not just to the average statistical properties of haloes.

Among the various available phenomenological models, we adopt the galaxy formation model of Mutch et al. (2013) (hereafter M13), since it allows us to compute the stellar mass assembly associated with the hierarchical growth of *individual* dark-matter haloes, hence accounting for the stochasticity of stellar mass growth in galaxies (e.g. see fig 1 of M13). In practice, the model of M13 relates the stellar mass growth in dark-matter haloes to two analytic functions: a ‘growth’ function, describing the amount of baryons available for star formation, and a ‘physics’ function, which determines the fraction of available baryons actually converted into stars. The variation of the stellar mass of a halo is therefore described by the following relation

$$\frac{dM_*}{dt} = F_{\text{growth}} F_{\text{phys}}, \quad (3)$$

where the growth function F_{growth} is defined as

$$F_{\text{growth}} = f_b \frac{dM_{\text{halo}}}{dt}, \quad (4)$$

where $f_b = 0.17$ is the universal fraction of baryons. The previous relation implies that the rate of change in the amount of available baryons is proportional to the rate of change in the virial mass of the halo, with the constant of proportionality being f_b .

We adopt a log-Cauchy function of halo mass to describe the

‘physics’ function, unlike M13 who adopt a log-normal function. The reason is that our study focuses on haloes of lower mass than those considered by M13, and the log-normal function proposed by M13 decays very rapidly far from the peak, implying an unphysical low efficiency of star formation at low halo masses. We therefore describe the ‘physics’ function as

$$F_{\text{phys}} = \epsilon \frac{\sigma^2}{(\log M_{\text{halo}} - \log M_{\text{vir}}^{\text{peak}})^2 + \sigma^2}, \quad (5)$$

and fix $\log(M_{\text{vir}}^{\text{peak}}/M_{\odot}) = 11.8$, $\sigma = 1$ and $\epsilon = 0.07$, all independent of redshift, to match the observed far-UV luminosity function of Bouwens et al. (2014) at $z = 7$ (see Section 3.3). Equation 5 implies an efficiency of baryons conversion into stars ~ 0.04 at $\log(M_{\text{halo}}/M_{\odot}) = 11$, and ~ 0.008 at $\log(M_{\text{halo}}/M_{\odot}) = 9$.

Equations (3)-(5) allow us to compute the star formation history from redshift 20 to 6.5 for all haloes identified in the Gaussian and non-Gaussian simulations. However, the M13 model does not include any prescription for the chemical evolution of galaxies, as they assume a constant value for the metallicity, 1/3 of the solar value, at all ages and galaxy masses. Unlike M13, we associate a value for the metallicity $[\text{Fe}/\text{H}](t)$ drawn from the mass-metallicity relation for dwarf galaxies of Kirby et al. (2013) (see their Eq. 4).

$$[\text{Fe}/\text{H}](t) = -1.69 + 0.3[\log(M_*/M_{\odot}) - 6], \quad (6)$$

assuming solar-scaled abundance ratios and a dispersion of 0.17 dex around this mean relation. This relation implies a metallicity $[\text{Fe}/\text{H}] = -1.54$ at $\log(M_*/M_{\odot}) = 6.5$ and $[\text{Fe}/\text{H}] = -0.79$ at $\log(M_*/M_{\odot}) = 9$.

2.4 Spectral evolution model

To compute the light emission from galaxies, we combine the star formation and chemical enrichment histories obtained with the M13 model with the population synthesis code of Bruzual & Charlot (2003). We adopt the Galactic-disc stellar initial mass function of Chabrier (2003), with lower and higher mass cut-offs at 0.1 and 100 M_{\odot} , respectively.¹

3 RESULTS

In the previous section, we have described the different N-body simulation we have run with Gaussian and non-Gaussian initial conditions, and the tools we have used to identify the dark matter haloes and build the merger trees. We have also described the M13 galaxy formation model, which we have used to compute the assembly of stellar mass with time in the dark matter haloes previously identified. Finally, we have introduced the BC03 population synthesis code, which we adopted to calculate the spectral energy distribution of each galaxy in the catalogues. With these tools we can compute the halo and stellar mass functions, and the far-UV luminosity function at different redshifts and for the different N-body simulation. In this section, we will show the results of these computations, showing the redshift evolution of these quantities for the Gaussian simulation, and the differences introduced by the primordial non-Gaussianities as a function of redshift and halo mass.

¹ The catalogues of halo masses, galaxy stellar masses and spectral energy distributions computed from the different Gaussian and non-Gaussian simulations in the redshift range $15 \leq z \leq 7$ are available upon request from the corresponding author.

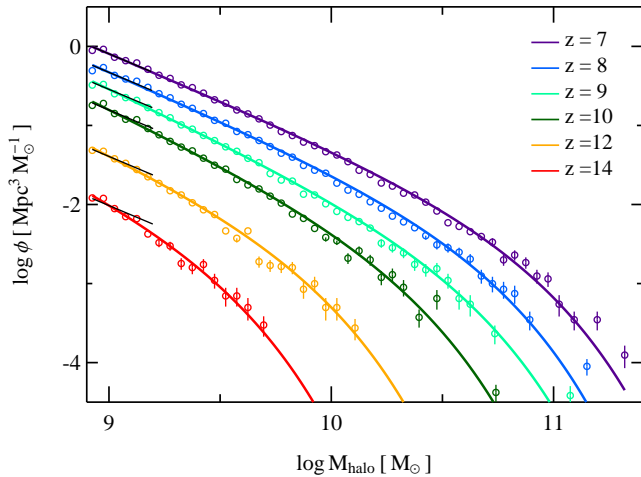


Figure 2. Halo mass function at different redshifts for the simulation with Gaussian initial conditions. Open circles indicate the mass function measured from our halo catalogue, while solid lines are a Schechter function fit to the points. Solid black lines are power laws $\Phi(M) \propto 10^{(M-M^*)(1+\alpha)}$ with α equal to the value obtained at $z = 7$ and scaled to match the computed mass functions at $\log(M_{\text{halo}}/M_{\odot}) = 9$, and are meant to highlight the evolution of the low-mass slope of the halo mass function with redshift. Error-bars are computed assuming independent Poisson distributions in each mass bin, and are plotted only when greater than the size of circles.

Results on the halo and stellar mass functions, and associated constraints, have been previously presented in Paper I, although assuming a different galaxy formation model.

3.1 Halo mass function

We show in Fig. 2 the evolution with redshift of the halo mass function obtained from the simulation with Gaussian initial conditions (see also paper I). The open circles of different colours represent the halo mass function at different redshifts measured from our simulation. To compute the halo mass function, we divide the halo catalogue in logarithmic mass bins of 0.05 dex width in the halo mass range $8.9 \leq \log(M_{\text{halo}}/M_{\odot}) \leq 11.4$, and then consider the number of haloes within each bin and divide this number by the simulation volume and bin width.² The limited volume of our simulations makes massive haloes rare, therefore increasing the Poisson noise at large halo masses. To reduce this noise, we merge adjacent bins until reaching ≥ 10 objects in each bin. Error-bars are computed assuming Poisson noise. The solid lines in Fig. 2 are obtained by fitting the binned luminosity function with a Schechter (1976) function of the form

$$\Phi(M) = \ln(10) \Phi^* 10^{(M-M^*)(1+\alpha)} \exp(-10^{M-M^*}), \quad (7)$$

where $M = \log(M_{\text{halo}}/M_{\odot})$, α is the slope of the power law at low masses, $M^* = \log(M_{\text{halo}}^*/M_{\odot})$ is the characteristic mass and Φ^* the normalisation. We adopt a Markov Chain Monte Carlo to find the combination of parameters M^* , α and Φ^* that best reproduce our measurements, choosing as best-fit values the median of

² We do not include satellite haloes in the computation of the halo mass function and in the successive computations. However, we note that the number of satellites at these redshifts is small, so the choice of including/neglecting them would not influence our results.

the posterior marginal distribution of each parameter. The adoption of an MCMC also allows us to derive reliable estimates on the uncertainties of the Schechter function parameters. To ease the comparison of the low-mass slope of the halo mass function we also over-plot with black lines in Fig. 2 a power law of the form $\Phi(M) \propto 10^{(M-M^*)(1+\alpha)}$ fixing α to the value obtained with the Schechter function fit at redshift $z = 7$ and normalising the function to match the measured mass function at $\log(M_{\text{halo}}/M_{\odot}) = 9$.

Fig. 2 indicates that the number density of haloes decreases with increasing redshift, at fixed halo mass, as expected in the hierarchical growth of structures in a Λ CDM Universe. The characteristic halo mass also decreases with increasing redshift, from $M^* = 10.78 \pm 0.05$ at $z = 7$ to $M^* = 9.39 \pm 0.12$ at $z = 14$. The low-mass slope of the halo mass function also evolves with redshift, becoming steeper with increasing redshift, from $\alpha = -2.19 \pm 0.02$ at $z = 7$ to $\alpha = -2.35 \pm 0.1$ at $z = 10$. At higher redshift, the smaller values of the characteristic halo mass M^* combined with the resolution of our simulation do not allow us to properly measure the slope of the low-mass end of the halo mass function, as the exponential cut-off of the mass function makes the fitted value α unreliable. The behaviour obtained for the halo mass function is expected in a Λ CDM Universe in which structures grow hierarchically from low to high masses, since merging increases, as the age of the Universe increases, the relative number of high mass haloes with respect to the low mass ones, thereby flattening the low-mass end of the mass function, while increasing the characteristic mass and number density of haloes.

We show in Fig. 3 the difference between the halo log-mass function computed from each simulation with non-Gaussian initial density perturbations and the simulation with Gaussian perturbations as a function of halo mass, for different redshifts (see also paper I). To accomplish this, we divide, at each redshift, the catalogue of halo masses of each simulation in 10 logarithmic bins in the range $8.9 \leq \log(M_{\text{halo}}/M_{\odot}) \leq 11.4$. We then divide the number of haloes in each bin by the simulation volume and bin width, obtaining the halo number density, and compute the difference $\delta\phi = (\log \phi_{\text{non-G}} - \log \phi_{\text{G}})$ between the halo number density for each non-Gaussian simulation and the Gaussian one as a function of halo mass. We only consider bins with ≥ 20 objects, and calculate the error in each bin by summing in quadrature the relative errors in the halo number density for the Gaussian and non-Gaussian simulation, which are in turn computed assuming a Poisson distribution. The different colours in Fig. 3 refer to different redshifts, and the width of the coloured regions reflects the error associated to each bin.

Fig. 3(a) indicates that the shallow spectrum ($\gamma = 1/2$), with a low normalisation ($f_{\text{NL}}^0 = 82$), used to generate the non-Gaussian initial conditions for the simulation non-G 1 produces a halo mass function which is statistically consistent with that obtained from the Gaussian simulation, at all redshift and halo masses.

Fig. 3(b) indicates that the steeper slope ($\gamma = 4/3$) and larger normalization ($f_{\text{NL}}^0 = 10^3$) adopted to generate the initial conditions for the non-G 2 simulation produces marginally larger differences in the halo mass function than those obtained for the non-G 1 model. These differences are < 0.1 dex at all redshift and halo masses here considered, and are more significant at low halo masses ($\log(M_{\text{halo}}/M_{\odot}) \lesssim 9.5$) because of the higher number of low- than high-mass haloes. We note also that the effect of initial non-Gaussianities increases with increasing redshift, at fixed halo mass.

Fig. 3(c) shows that the non-G 3 model ($\gamma = 2$ and $f_{\text{NL}}^0 = 7.357 \times 10^3$), which has stronger initial non-Gaussianities than the

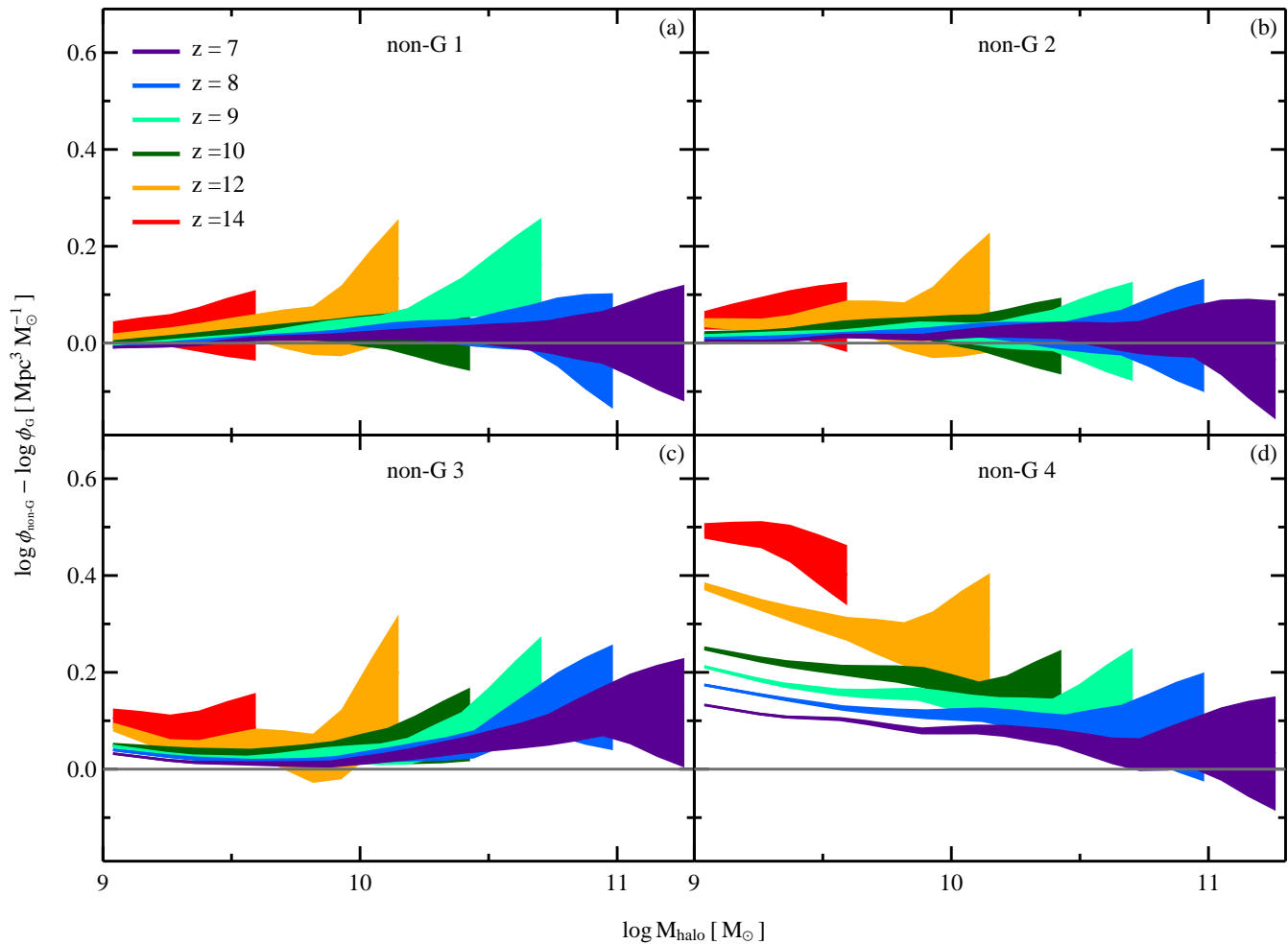


Figure 3. Impact of primordial non-Gaussianities on the halo mass function. (a) Difference between the halo mass function computed from the non-Gaussian simulation 1 and that computed from the Gaussian simulation, at redshift $z = 7$ (purple region), 8 (blue), 9 (light green), 10 (dark green), 12 (orange), 14 (red). (b) Same as (a), but for the non-Gaussian simulation 2. (c) Same as (a), but for the non-Gaussian simulation 3. (d) Same as (a), but for the non-Gaussian simulation 4. Each coloured region is computed assuming independent Poisson errors for each simulation and mass bin (see Section 3.1).

non-G 1 and 2 models, produces statistically significant variations in the halo mass function (up to 0.2 dex) with respect to the Gaussian simulation, at all redshifts and both at low and high masses. At fixed redshift, the non-G 3 halo mass function deviates the most from the Gaussian mass function at the extreme of the mass range, while being more similar at $\log(M_{\text{halo}}/M_{\odot}) \sim 10$; i.e. the effect of the primordial non-Gaussianities in this model is to increase the number of both low- and high-mass haloes. As for the non-G 2 simulation, these deviations become more statistically significant at low halo masses because of the larger number of low- than high-mass haloes in our simulation volume. We note also that at fixed halo mass the difference between the non-G 3 and Gaussian halo mass function increases with increasing redshift, following the same qualitative trend observed for the non-G 2 simulation.

Fig. 3(d) indicates that the halo mass function of the non-G 4 model ($\gamma = 4/3$ and $f_{\text{NL}}^0 = 10^4$) exhibits differences up to ~ 0.5 dex with respect to that of the Gaussian simulation. These differences are much larger, at all redshift and halo masses, than those observed for the non-G 1, non-G 2 and non-G 3 simulations. This behaviour is expected, as the non-G 4 simulation has the strongest level of primordial non-Gaussianities at scales $\log(k/\text{Mpc}) < 2$ with respect to all other non-Gaussian models adopted in this work (see Fig. 1). At

fixed mass, the number of low-mass haloes increases with increasing redshift with respect to the Gaussian simulation, in a consistent manner to what obtained for the non-G 1, non-G 2 and non-G 3 simulations. At fixed redshift, the difference in the number density of haloes with respect to the Gaussian simulation increases with decreasing halo mass, unlike the results from the non-G 3 simulation.

The trends shown in Fig. 3 for the different non-Gaussian models can be understood as follows. First of all, a (scale-independent) positive skewness in the matter fluctuations boosts the formation of rare objects, i.e. massive haloes, since it increases their probability to cross the threshold density contrast required for collapse (e.g. Matarrese et al. 2000). However, adopting a scale-dependent skewness complicates this picture, as for ‘blue’ tilts, i.e. a skewness that increases with decreasing scale, the formation of low mass haloes is also amplified. The reason is that in these models the skewness is larger on smaller scales, those corresponding to small-scale fluctuations, i.e. to low mass haloes. The net effect of a scale-dependent primordial non-Gaussianity with a ‘blue’ spectrum is therefore the combination of these two effects: a boost of rare fluctuations (i.e. massive haloes), and an increasingly stronger boost of fluctuations with decreasing scale, i.e. decreasing halo mass, with the relative strengths of these effects being determined

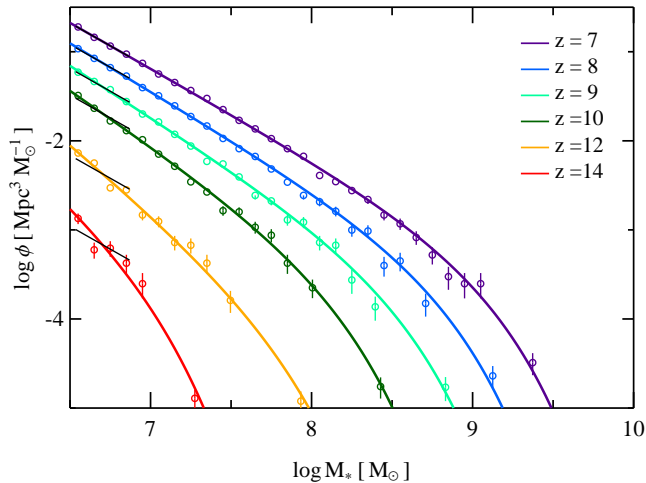


Figure 4. Galaxy stellar mass function at different redshifts for the simulation with Gaussian initial conditions. Open circles indicate the stellar mass function computed from our simulation, while solid coloured lines are fit to the points with a Schechter function. Solid black lines are power laws $\Phi(M) \propto 10^{(M-M^*)(1+\alpha)}$ with α equal to the value obtained at $z = 7$ and scaled to match the computed mass functions at $\log(M_*/M_\odot) = 6.7$. Error bars are computed assuming independent Poisson distributions in each mass bin, and are plotted only when greater than the size of circles.

by the shape and normalisation of the adopted model for the non-Gaussianity.

In the next section we will show how the effect of primordial non-Gaussianities on the number density of haloes at different redshifts affects the redshift evolution of the galaxy stellar mass function.

3.2 Galaxy stellar mass function

We have shown that the adoption of non-Gaussian initial density perturbations produces measurable differences in the halo mass function for the non-Gaussian simulations 2, 3 and 4, i.e. for those simulations with strong enough initial non-Gaussianities. We therefore expect a similar behaviour for the galaxy stellar mass function, as it depends on the halo merger history (see equations (3)-(5)).

We show in Fig. 4 the galaxy stellar mass function obtained by applying the galaxy formation model of M13 (see Section 2.3) on the dark-matter simulation with Gaussian initial conditions. The open circles of different colours indicate the mass function at different redshifts. We compute the galaxy stellar mass function in the same way as we do for the halo mass function (see Section 3.1), but adopting logarithmic mass bins of 0.1 dex width in the range $6.5 \leq \log(M_*/M_\odot) \leq 10$. The solid, coloured lines in Fig. 4 are obtained by fitting a Schechter function to our measured points (see equation (7) and Sec. 3.1 for details). The solid black lines in Fig. 4 are power laws of the form $\Phi(M) \propto 10^{(M-M^*)(1+\alpha)}$ with α equal to the value obtained with the Schechter function fit at redshift $z = 7$, and normalised to match the measured stellar mass function at $\log(M_*/M_\odot) = 6.7$.

Fig. 4 shows that, as for the halo mass function of Fig. 2, the number density of galaxies decreases with increasing redshift, at fixed stellar mass. The characteristic stellar mass also decreases with increasing redshift, from $M^* = 9.03 \pm 0.12$ at $z = 7$ to $M^* = 6.90 \pm 0.36$ at $z = 14$, indicating that the typical stellar mass of galaxies decreases with increasing redshift. The low-mass

end of the mass function steepens with increasing redshift, from $\alpha = -2.03 \pm 0.02$ at $z = 7$ to $\alpha = -2.23 \pm 0.07$ at $z = 10$. As we already noted for the halo mass function, at higher redshift the low values of the characteristic stellar mass combined with the resolution of the N-body simulation makes the exponential cut-off important at all stellar masses here considered, therefore affecting the value of α obtained with the Schechter function fit. The likely explanation for the flattening of the low-mass end of the stellar mass function from high to low redshift is merging, as we already noted for the halo mass function. We note also that at a given redshift the low-mass slope of the stellar mass function is flatter than the halo mass function ($\alpha_{\text{halo}} - \alpha_{\text{star}} \sim 0.15$ at $z = 7-10$). This is due to the increasing efficiency of baryon conversion into stars with increasing halo mass in the galaxy formation model adopted in this work, for the halo mass ranges here considered (see Section 2.3 and equation 5). This causes high mass haloes to have, on average, larger stellar-to-halo mass ratios (M_*/M_{halo}) than haloes with lower mass, thus increasing the relative number of high- to low-mass galaxies, i.e. flattening the stellar mass function with respect to the halo mass function.

We show in Fig. 5 the effect of non-Gaussian initial density perturbations on the galaxy stellar mass function as a function of stellar mass. We compute the stellar mass function for the Gaussian simulation and each non-Gaussian simulation in the same way as we do for the halo mass function (see Section 3.1), adopting 10 logarithmic bins in the range $6.5 \leq \log(M_*/M_\odot) \leq 10$, and considering only bins with ≥ 20 objects.

Fig. 5(a) displays the difference between the galaxy stellar mass function computed from the non-G 1 simulation and that computed from the Gaussian simulation. As for the halo mass function [see Fig. 3(a)], the stellar mass function obtained from the non-G 1 model is consistent, within the errors, with that computed from the Gaussian simulation, at all redshift and masses.

Fig. 5(b) indicates that, unlike the galaxy stellar mass function of the non-G 1 simulation, that of the non-G 2 simulation exhibits, at low ($\log(M_*/M_\odot) \lesssim 8$) masses, small (< 0.1 dex) but statistically significant differences with the mass function of the Gaussian simulation. In particular, the number of low-mass galaxies is increased with respect to the Gaussian simulation. Also, this effect increases with increasing redshift, at fixed stellar mass, as already noted for the halo mass function (Section 3.1).

Fig. 5(c) shows that the primordial non-Gaussianities adopted in the non-G 3 simulation, stronger than those in the non-G 1 and non-G 2 simulations, produce even more statistically significant differences with respect to the stellar mass function of the Gaussian simulation, both at low and high stellar masses. At each redshift, the number density of low- and high-mass galaxies is increased with respect to the Gaussian simulation, but, unlike the corresponding figure for the halo mass function [Fig. 3(c)], the effect is more pronounced for high-mass galaxies. We can explain this behaviour by appealing to the decreasing efficiency of baryon conversion into stars, i.e. the decrease of the stellar-to-halo mass ratio, with decreasing halo mass, which reduces the differences between the non-G 3 and Gaussian simulations at low stellar masses. At fixed stellar mass, the effect of primordial non-Gaussianities on the galaxy stellar function increases with increasing redshift, as we already noted for the non-G 2 simulation.

Fig. 5(d) indicates that the non-G 4 simulation, which has the strongest level of primordial non-Gaussianities among all simulations, produces the strongest deviations in the galaxy stellar mass function with respect to the Gaussian simulation, as already noted for the halo mass function in Fig. 3(d). At all redshift and masses

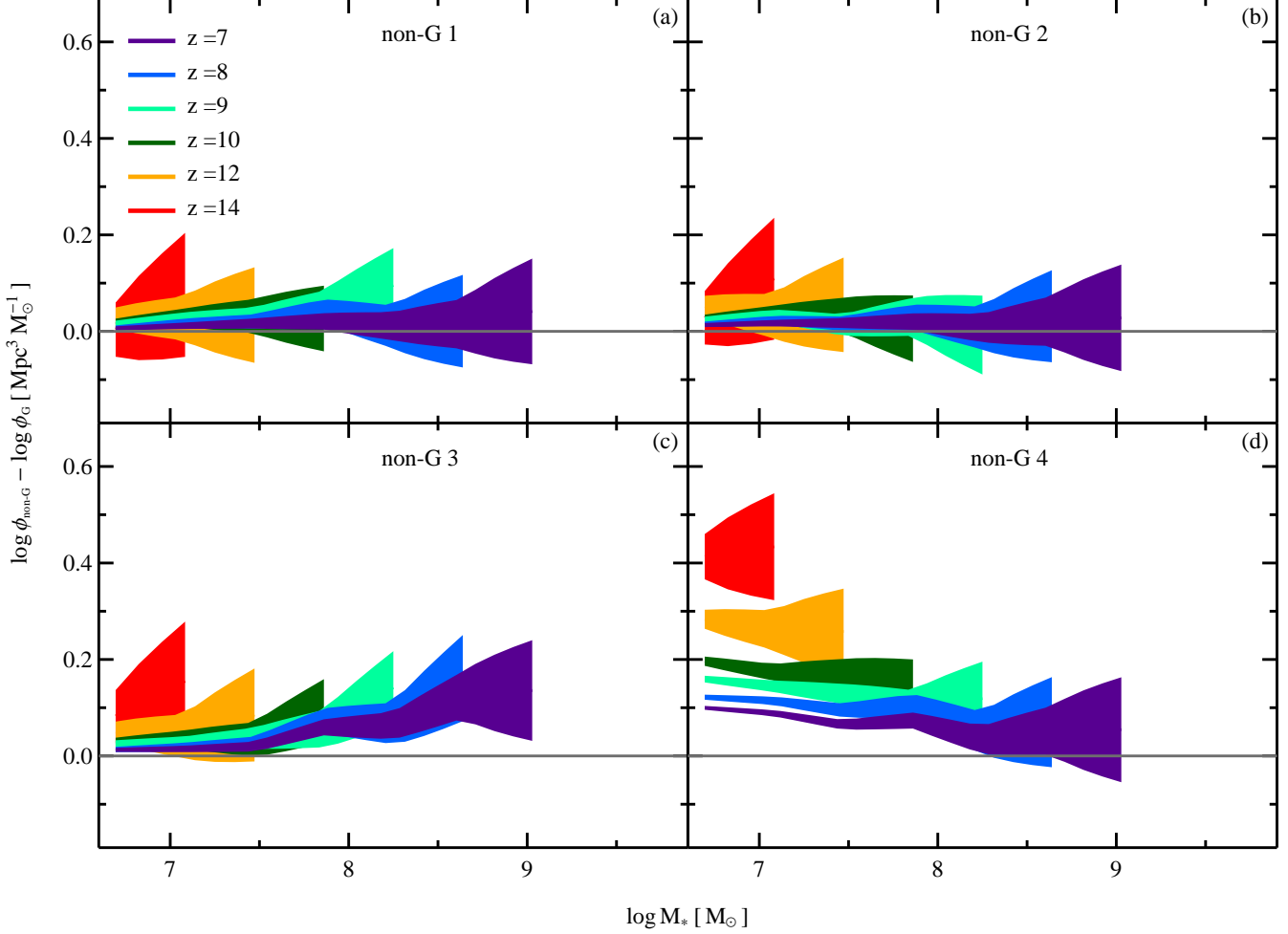


Figure 5. Impact of primordial non-Gaussianities on the galaxy stellar mass function. (a) Difference between the galaxy stellar mass function computed from the non-Gaussian simulation 1 and that computed from the Gaussian simulation, at redshift $z = 7$ (purple region), 8 (blue), 9 (light green), 10 (dark green), 12 (orange), 14 (red). (b) Same as (a), but for the non-Gaussian simulation 2. (c) Same as (a), but for the non-Gaussian simulation 3. (d) Same as (a), but for the non-Gaussian simulation 4. Each coloured region is computed assuming independent Poisson errors for each simulation and mass bin.

the number density of galaxies is larger in the non-G 4 simulation than in the Gaussian simulation. This difference increases, at fixed stellar mass, with increasing redshift, reaching $\delta\phi \sim 0.4$ at $z = 14$ and $\log(M_*/M_\odot) = 6.5$. We note that this value is lower than that observed in the halo mass function [$\delta\phi \sim 0.5$, see Fig. 3(d)], and that, even though at fixed redshift the difference between the non-Gaussian and Gaussian mass functions increases with decreasing galaxy stellar mass, this trend is weaker (i.e. flatter) than that for the halo mass function. This is in qualitative agreement to what we noted for the non-G 3 simulation and likely related to the same explanation: the decreasing baryon conversions efficiency with decreasing halo mass reduces the differences between the non-Gaussian simulations and the Gaussian one at low stellar masses.

Our results on the effects of non-Gaussianity on the galaxy stellar mass function are qualitatively very similar to those found in paper I, despite the different galaxy formation models used (see fig 3 of Habouzit et al. 2014).

In the next section, we will show by means of the Bruzual & Charlot (2003) population synthesis code how the differences in the galaxy stellar mass function between the non-Gaussian and Gaussian simulations reflect into different far-UV luminosity functions at different redshifts.

3.3 UV luminosity function

In the previous sections we have illustrated the effect of primordial non-Gaussianities on the halo and stellar mass functions computed from our N-body simulation and the M13 galaxy formation model. By means of the galaxy chemical evolution prescription presented in Section 2.3 (see Equation 6) and the Bruzual & Charlot (2003) population synthesis code, we now show the effect of non-Gaussian initial density perturbations on the redshift evolution of the far-UV luminosity function.

Fig. 6 shows the far-UV luminosity function computed from the Gaussian simulation. The open circles of different colours indicate the far-UV luminosity function at different redshifts, which we compute in the same way as we do for the halo mass function (see Section 3.1), but adopting bins of far-UV absolute magnitudes 0.2 dex width in the range $-22 \leq M_{\text{FUV}} \leq -14$. The solid, coloured lines in Fig. 6 are computed by fitting with the same method outlined in Sec. 3.1 a Schechter function of the form

$$\phi(M) = 0.4 \ln(10) \phi^* 10^{-0.4(M-M^*)(1+\alpha)} \exp\left(-10^{-0.4(M-M^*)}\right), \quad (8)$$

where $M = M_{\text{FUV}}$ is the far-UV absolute magnitude, α is the slope

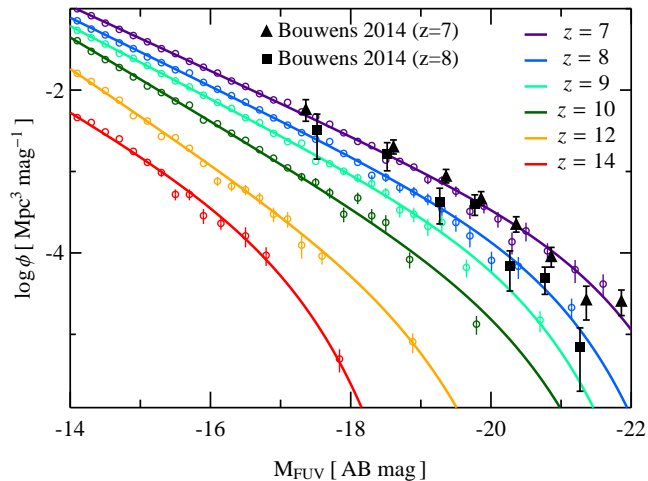


Figure 6. Far-UV luminosity function at different redshifts for the simulation with Gaussian initial conditions. Open circles indicate the far-UV luminosity function computed from our simulation, while solid coloured lines are fit to the points with a Schechter function. Error-bars are computed assuming independent Poisson distributions in each mass bin, and are plotted only when greater than the size of circles. Black-filled symbols indicate the UV luminosity function measured by Bouwens et al. (2014) at $z \sim 7$ (598 galaxies, triangles) and $z = 8$ (225 galaxies, squares).

of the power law at low luminosities, M^* is the characteristic magnitude and ϕ^* the normalisation.

We also show in Fig. 6 the far-UV luminosity function computed by Bouwens et al. (2014) using 598 galaxies at $z \sim 7$ (black triangles) and 225 galaxies at $z \sim 8$ (black square). Fig. 6 shows that our simple galaxy formation model (see Section 2.3) reproduces well the observed far-UV luminosity function at $z = 7$ and 8. This is quite a remarkable result, as by tuning the free parameters of the model to match the data at $z = 7$ we naturally obtain prediction in agreement with $z = 8$ observations. This indicates that our simple model, based on just three adjustable parameters, is able to subsume the complex physics of star formation at these redshifts, and that there is no need for a redshift evolution of the model parameters from $z = 7$ to 8. We note that the Bouwens et al. (2014) data are not corrected for dust attenuation, but, as we discuss in Section 6.3, we do not expect dust corrections to be significant at these redshifts for most galaxy luminosities considered here.

It is important to highlight that although we calibrate the galaxy formation model with the predictions from the Gaussian simulation, this calibration is valid for the non-Gaussian simulations too. The reason is that the effect of the initial non-Gaussianities adopted in this work decreases with decreasing redshift, hence the galaxy luminosity functions at $z = 7$ and 8 are almost indistinguishable among the different simulations (see Fig. 8). This guarantees the consistency of the non-Gaussian simulations with the Bouwens et al. (2014) observational constraints.

Fig. 6 shows that the number density of galaxies decreases with increasing redshift, at fixed far-UV absolute magnitude, in a qualitatively similar way to what we have already shown for the halo and stellar mass function (see Sec. 3.1–3.2). The characteristic far-UV magnitude also decreases with increasing redshift, from $M_{\text{FUV}}^* = -21.3 \pm 0.37$ at $z = 7$ to $M_{\text{FUV}}^* = -16.7 \pm 0.4$ at $z = 14$, indicating that luminous galaxies become rarer and rarer at higher redshift. The faint-end end of the luminosity function steepens with increasing redshift, from $\alpha = -1.99 \pm 0.01$ at $z = 7$ to $\alpha = -2.28 \pm 0.04$ at $z = 10$ (see Fig. 7). At higher redshift, the low values of the char-

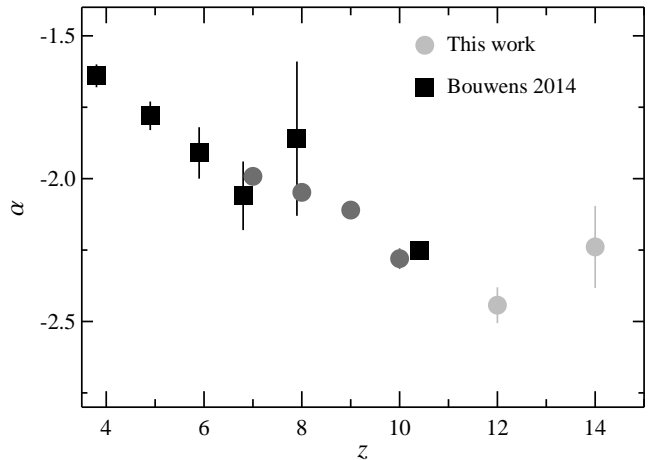


Figure 7. Evolution with redshift of the faint-end slope of the far-UV luminosity function. Black squares indicate the slope of the UV luminosity function as measured by Bouwens et al. (2014) at $z = 7$ and 8, while grey circles show the value of α computed from our galaxy formation model applied to the dark matter simulation with Gaussian initial conditions. In light grey, we indicate the allowed values of α , which are more uncertain because of the combined effects of the low value of the characteristic far-UV magnitude and limited resolution of our simulation (see Section 3.3). Note that Bouwens et al. (2014) fix the value of $\alpha = -2.25$ at $z \sim 10$ when fitting a Schechter function to their data.

acteristic magnitude make the exponential cut-off important at all stellar magnitudes considered here, therefore making the value of α in the Schechter function fit more uncertain. The flattening of the far-UV luminosity function from high to low redshift reflects the one already observed for the halo and stellar mass functions, and is likely caused by the same mechanism, i.e. galaxy merging.

A crucial factor for any model of Universe reionization based on star-forming galaxies is the faint-end slope of the far-UV luminosity function, since it determines the relative ‘weight’ of low- and high-mass galaxies on the production rate of hydrogen-ionizing photons (see Equation 12). For this reason, we compare in Fig. 7 the predicted evolution with redshift of the faint-end slope of the luminosity function of our model with the measurements of Bouwens et al. (2014). Fig. 7 shows that our model predictions agree remarkably well with the Bouwens et al. (2014) measurements at $z \sim 7 - 10$. At $z \gtrsim 10$, our predictions for the evolution of α are influenced by the exponential cut-off of the Schechter function and are therefore less reliable. We also note that the choice of Bouwens et al. (2014) to fix the value of $\alpha = -2.25$ when fitting a Schechter function to their $z = 10$ galaxy candidates is supported by our model predictions. As we noted above for the far-UV luminosity function, the convergence of the predictions obtained from the non-Gaussian simulations towards those of the Gaussian simulation at $z \lesssim 8$ guarantees the evolution of α with redshift of the non-G models to be in agreement with the Bouwens et al. (2014) measurements.

As for the halo and stellar mass functions, we show in Fig. 8 the effect of primordial non-Gaussianities on the far-UV galaxy luminosity function. To accomplish this, we compute the far-UV luminosity function for the Gaussian simulation and each non-Gaussian simulation in the same way as we do for the halo mass function (see Section 3.1), adopting 10 bins in the range $-22 \leq M_{\text{FUV}} \leq -14$, and considering only bins with ≥ 20 objects.

Fig. 8(a) shows that the far-UV luminosity function computed

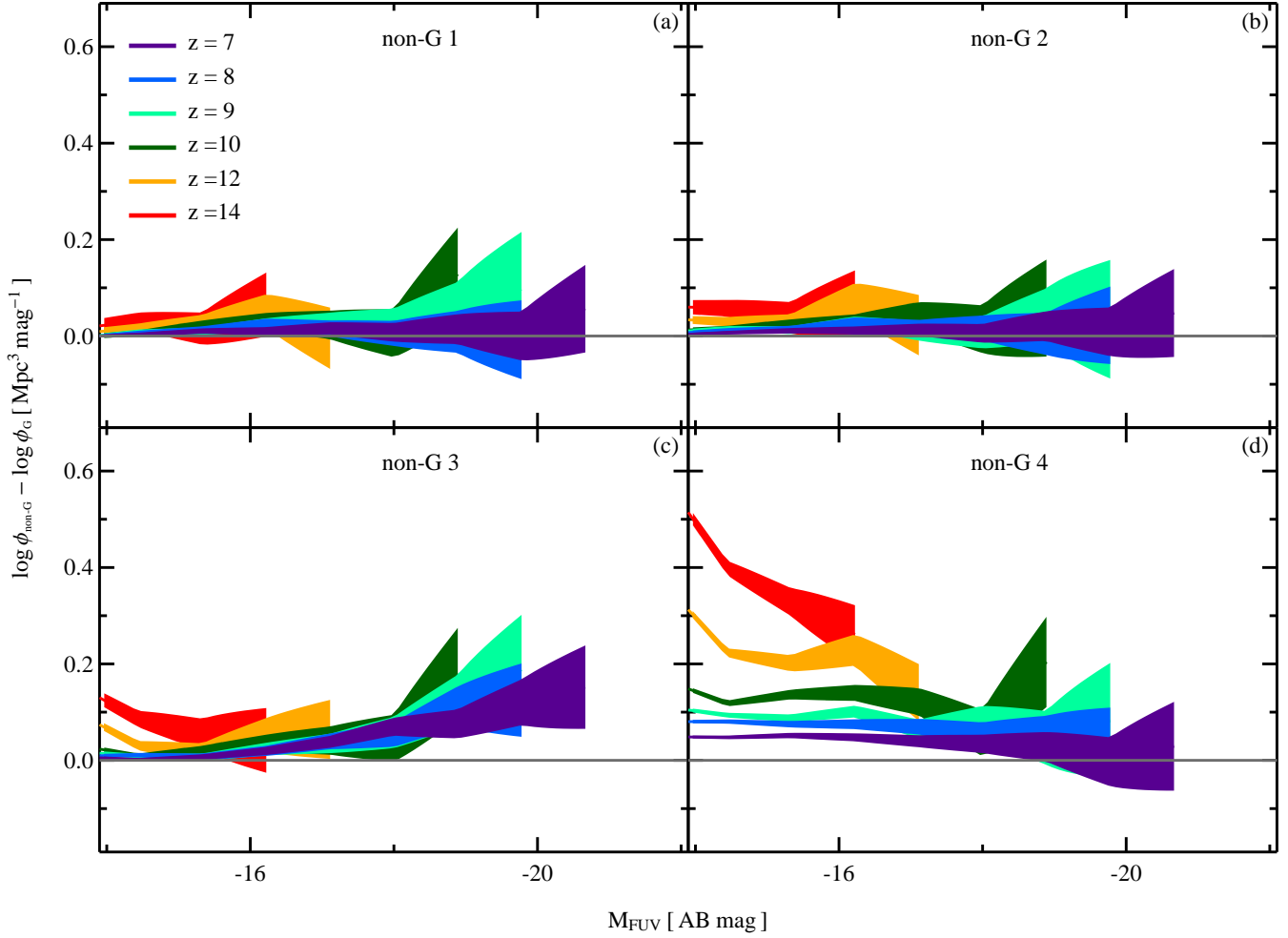


Figure 8. Impact of primordial non-Gaussianities on the far-UV luminosity function. (a) Difference between the far-UV luminosity function computed from the non-Gaussian simulation 1 and that computed from the Gaussian simulation, at redshift $z = 7$ (purple region), 8 (blue), 9 (light green), 10 (dark green), 12 (orange), 14 (red). (b) Same as (a), but for the non-Gaussian simulation 2. (c) Same as (a), but for the non-Gaussian simulation 3. (d) Same as (a), but for the non-Gaussian simulation 4. Each coloured region is computed assuming independent Poisson errors for each simulation and mass bin.

from the non-G 1 simulation and that computed from the Gaussian simulation are consistent at all redshifts and magnitudes, as we already noted for the halo and stellar mass functions.

Fig. 8(b) indicates that the number density of faint galaxies ($M_{\text{FUV}} \gtrsim -17$) is marginally larger in the non-G 2 simulation than in the Gaussian simulation. As we have already noted for the halo and galaxy stellar mass functions (see Figs. 3(b) and 5(b)), this effect becomes stronger, at fixed far-UV absolute magnitude, with increasing redshift, reaching $\delta\phi \sim 0.07$ at $z = 14$.

As we consider models with stronger initial non-Gaussianities, the effect of such non-Gaussianities on the far-UV luminosity function becomes stronger, as already noted for the halo and stellar mass functions. Fig. 8(c) indeed shows significant differences between the non-G 3 and Gaussian far-UV luminosity function. The number density of galaxies is larger for the non-G 3 model than for the Gaussian one both at the faint and bright end of the luminosity function, and at all redshifts. At the bright end of the luminosity function the large Poisson errors do not allow us to identify trend with redshift. At $M_{\text{FUV}} \gtrsim -15$ the effect of non-Gaussianities becomes stronger with increasing redshift, at fixed far-UV absolute magnitude, reaching $\delta\phi \sim 0.15$ at $z = 14$.

As for the halo and stellar mass functions, Fig. 8(d) shows that the non-G 4 model, which has the strongest initial non-Gaussianities, produces the largest differences in the far-UV luminosity function. The number density of galaxies is larger in the non-G 4 model than in the Gaussian model at all redshift and magnitudes. We also recover the same trends with redshift and mass (here luminosity) already found for the halo and stellar mass functions, as the differences introduced by non-Gaussianities increases with increasing redshift, at fixed far-UV absolute magnitude, reaching $\delta\phi \sim 0.5$ at $z = 14$. At fixed redshift, the difference between the non-G 4 and Gaussian far-UV luminosity function increases with increasing absolute magnitude, i.e. with decreasing galaxy luminosity.

In the next section, we present the reionization model we adopt to study how the differences in the far-UV luminosity function introduced by primordial non-Gaussianities might affect the reionization history of the Universe.

4 REIONIZATION MODEL

We can describe cosmic reionization with a differential equation accounting for the competing processes of hydrogen ionization by Lyman-continuum photons (with $E > 13.6$ eV) and hydrogen recombination (e.g. Madau et al. 1999)

$$\frac{dQ_{\text{HII}}}{dt} = \frac{\dot{n}_{\text{ion}}}{\langle n_{\text{H}} \rangle} - \frac{Q_{\text{HII}}}{t_{\text{rec}}}, \quad (9)$$

where Q_{HII} expresses the volume filling fraction of ionized hydrogen, \dot{n}_{ion} the comoving production rate of hydrogen ionizing photons, $\langle n_{\text{H}} \rangle$ the comoving average number density of hydrogen atoms, and t_{rec} the average recombination time of hydrogen. Note that Equation 9 does not account for collisional ionization and implicitly assumes that the ionization sources are widely separated, as it mixes mass-averaged (ionization fraction) and volume-averaged (recombination time) quantities (see the discussion in section 5 of Finlator et al. 2012).

The comoving average number density of hydrogen atoms (n_{H}) (units of cm^{-3}) can be expressed as

$$\langle n_{\text{H}} \rangle = \frac{X_{\text{p}} \Omega_{\text{b}} \rho_{\text{c}}}{m_{\text{H}}},$$

where $X_{\text{p}} = 0.75$ indicates the primordial mass-fraction of hydrogen (e.g. Coc et al. 2013), $\rho_{\text{c}} = 1.8787 \times 10^{-29} h^{-2} \text{ g cm}^3$ the critical density of the Universe, $\Omega_{\text{b}} = 0.052$ the fractional baryon density (assuming *Planck* values for $\Omega_{\text{m}} = 0.307$ and a baryon fraction $f_{\text{b}} = 0.17$), and $m_{\text{H}} = 1.6735 \times 10^{-24} \text{ g}$ the hydrogen mass.

We assume that reionization is driven solely by UV radiation emitted by massive stars in early galaxies, therefore neglecting any contribution from other ionization sources, such as Pop III stars and quasars (see Section 6.1 for a discussion). Under this assumption, we can express the production rate of Lyman-continuum photons as

$$\dot{n}_{\text{ion}} = f_{\text{esc}} \xi_{\text{ion}} \rho_{\text{UV}}, \quad (10)$$

where f_{esc} is the fraction of Lyman-continuum photons escaping the interstellar medium (ISM) of the galaxy in which they are produced, ξ_{ion} the rate of Lyman-continuum photons per unit UV luminosity (computed at 1500 Å), and ρ_{UV} the UV galaxy luminosity density. In the most general case, f_{esc} , ξ_{ion} and ρ_{UV} are redshift and luminosity dependent, but in this work we will consider f_{esc} and ξ_{ion} independent on the galaxy luminosity. This is motivated, for ξ_{ion} , by Fig. 9, which shows that the production rate of Lyman-continuum photons by galaxies with luminosity in the range $-22 \leq M_{\text{FUV}} \leq -14$ varies by $\lesssim 0.15$ dex at fixed redshift. We can therefore adopt a constant value of ξ_{ion} in each redshift bin. In practice, we compute the median value of ξ_{ion} in each redshift bin for galaxies with luminosities in the range $-22 \leq M_{\text{FUV}} \leq -14$, and report in Table 2 the value obtained for the Gaussian and non-Gaussian simulations. As Table 2 shows, at each redshift we obtain the same median value of ξ_{ion} for the Gaussian and non-Gaussian simulation 1, 2 and 3, and slightly lower values for the non-Gaussian simulation 4.

The fraction of Lyman-continuum photons escaping their galaxies is one of the most uncertain ingredients of current reionization models, since there is no direct observational constraint on this quantity (see Section 6.2.1 for a discussion). We therefore adopt two different scenarios, one in which the escape fraction is constant with redshift ($f_{\text{esc}} = 0.2$), the other in which f_{esc} varies with redshift. We note that assuming an escape fraction increasing

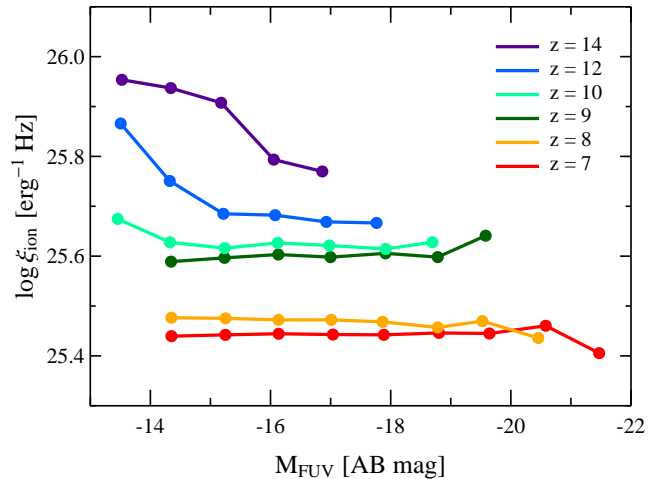


Figure 9. Median value of the production rate of Lyman-continuum photons $\log \xi_{\text{ion}}$ as a function of the FUV absolute magnitude, at different redshifts, obtained from the spectral energy distributions of the galaxies in the Gaussian simulation. At fixed redshift, $\log \xi_{\text{ion}}$ exhibits variations $\lesssim 0.15$ dex in the luminosity range $-22 \leq M_{\text{FUV}} \leq -14$.

Redshift	$\log \xi_{\text{ion}} [\text{erg}^{-1} \text{Hz}]$	
	G, non-G 1, 2 and 3	non-G 4
7	25.44	25.43
8	25.47	25.46
9	25.59	25.57
10	25.62	25.60
12	25.72	25.68
14	25.93	25.83

Table 2. Production rate of hydrogen ionizing photons ($E > 13.6$ eV) computed from the different Gaussian and non-Gaussian simulations. For each simulation, we compute the values listed in the table by dividing the galaxies in redshift bins, then considering the median value of ξ_{ion} for all galaxies with UV luminosity in the range $-22 \leq M_{\text{FUV}} \leq -14$.

with redshift is equivalent to assuming f_{esc} increases with decreasing galaxy luminosity (or halo mass), once photoionization quenching and the evolution of the luminosity function are taken into account (Alvarez et al. 2012). We adopt the dependence of f_{esc} on redshift of Kuhlen & Faucher-Giguère (2012) and Robertson et al. (2013)

$$f_{\text{esc}}(z) = f_{\text{esc}}^0 \left(\frac{1+z}{5} \right)^k, \quad (11)$$

where we fix $f_{\text{esc}}^0 = 0.054$ and $k = 2.4$, following Robertson et al. (2013). This equation implies an escape fraction $f_{\text{esc}} = 0.17$ at $z = 7$ and $f_{\text{esc}} = 0.75$ at $z = 14$, in qualitative agreement with the values obtained from state-of-the-art simulations by other groups (e.g. Paardekooper et al. 2013; Wise et al. 2014; So et al. 2014).

We compute the UV luminosity density ρ_{UV} by analytically integrating the Schechter fit to the UV luminosity function obtained from our galaxy formation model applied to the different Gaussian

and non-Gaussian simulation (see Section 3.3), obtaining

$$\begin{aligned} \rho_{\text{UV}} &= \int_{-\infty}^{M_{\text{FUV}}^{\text{lim}}} \phi(M)L(M)dM \\ &= \phi^* M^* \Gamma(\alpha + 2, M_{\text{FUV}}^{\text{lim}}/M^*), \end{aligned} \quad (12)$$

where $\Gamma(\alpha + 2, M_{\text{FUV}}^{\text{lim}}/M^*)$ is the upper Incomplete Gamma function. The result of the integration depends on the parameters of the Schechter function ϕ^* , M^* and α , which we derive by means of an MCMC fitting of Equation 8 to the binned luminosity function of each simulation at each redshift, and on the minimum galaxy luminosity $M_{\text{FUV}}^{\text{lim}}$.

The minimum galaxy luminosity is also an uncertain ingredient of any reionization model, as current observations of high redshift galaxies probe only the bright end of the UV luminosity function (see Section 6.2.2 for a discussion). This value depends on the minimum mass of a halo able to cool down the gas to the temperatures required for star formation, and therefore on the highly uncertain physics of high redshift dwarf galaxy formation models (e.g. effects of cooling from molecular hydrogen and metal lines, UV background, stellar feedback, see Wise et al. 2014). As for the escape fraction, we have to rely on simulations and previous work. We therefore fix $M_{\text{FUV}}^{\text{lim}} = -12$ (AB magnitude), which is, for instance, similar to the preferred value of Robertson et al. (2013), and consistent with the recent simulations of Wise et al. (2014), in which galaxies down to $M_{\text{FUV}}^{\text{lim}} \sim -5$ are formed. Since our model galaxies of $M_{\text{FUV}} = -14$ correspond to haloes of $10^9 M_{\odot}$, adopting a limiting far-UV magnitude of -12 is equivalent to considering halo masses down to $\sim 10^8 M_{\odot}$, assuming a fixed mass-to-light ratio in this mass range. Note that, unlike Robertson et al. (2013), we do not adopt a single metallicity to compute the spectral energy distribution of our model galaxies, since we adopt the mass-metallicity relation for dwarf galaxies of Kirby et al. (2013) to calculate the chemical evolution of all galaxies in our simulations (see Section 2.3).

The last quantity entering Equation 9 is the average recombination time of ionized hydrogen atoms in the IGM, which is

$$\begin{aligned} t_{\text{rec}} &= [\alpha_{\text{B}}(T)n_{\text{e}}]^{-1} \\ &= \left[C_{\text{HII}}\alpha_{\text{B}}(T)f_{\text{e}}\langle n_{\text{H}} \rangle (1+z)^3 \right]^{-1}, \end{aligned} \quad (13)$$

where α_{B} is the hydrogen recombination coefficient, $n_{\text{e}} = f_{\text{e}} \langle n_{\text{H}} \rangle (1+z)^3$ the number density of free electrons at redshift z , f_{e} the fraction of free electrons per hydrogen nucleus in the ionized IGM, and C_{HII} the ‘clumping factor’, which accounts for inhomogeneities in the reionization process. We adopt an electron temperature of $T = 20000$ K and adopt the case B recombination coefficient $\alpha_{\text{B}} = 2.52 \times 10^{-13} \text{ cm}^3 \text{ s}^{-1}$.³ Assuming that helium is doubly ionized at $z < 4$ and singly ionized at higher redshift (e.g. Kuhlen & Faucher-Giguère 2012), we can express the number of free electrons per hydrogen nucleus as

$$f_{\text{e}} = \begin{cases} 1 + Y_{\text{p}}/2X_{\text{p}} & \text{at } z \leq 4, \\ 1 + Y_{\text{p}}/4X_{\text{p}} & \text{at } z > 4, \end{cases}$$

where X_{p} and $Y_{\text{p}} = 1 - X_{\text{p}}$ indicate the primordial mass fraction of hydrogen and helium, respectively.

The clumping factor that enters the recombination time allows

Reionization model	f_{esc}	$M_{\text{FUV}}^{\text{lim}}$
A	0.2	-12
B	increasing with z (see Equation 11)	-12
C	increasing with z (see Equation 11)	-7

Table 3. Different reionization models adopted in this work. We adopt for all models the clumping factor of Finlator et al. (2012) (see Equation 14), while we vary the escape fraction and limiting UV magnitude. Note that for model C we consider a limiting magnitude of -7, but adopting a constant number density of galaxies in the range $-12 \leq M_{\text{FUV}} \leq -7$, equal to the density at $M_{\text{FUV}} = -12$.

one to account for the effect of inhomogeneities in the density, temperature and ionization fields of the IGM. As for the escape fraction, one has to rely on simulations, since there are no observational constraints on the quantities determining the recombination rate of the IGM at high redshift (see Section 6.2.3 for a discussion). We adopt for C_{HII} the analytic expression of Finlator et al. (2012), which is based on state-of-the-art hydrodynamical simulations which include the effect of stellar feedback, photo-heating from a UV background, and self-shielding on the IGM:

$$C_{\text{HII}} = 9.25 - 7.21 \log(1+z), \quad (14)$$

which implies a clumping factor that increases from 0.77 at $z = 14$ to 3.16 at $z = 6$. Note that Equation 14 is in excellent agreement to that found by Wise et al. (2014) in their recent hydrodynamical simulations.

An important constraint on cosmic reionization comes from the optical depth of electrons to Thomson scattering, which can be expressed as

$$\tau_e = \int_0^{\infty} dz \frac{c(1+z)^2}{H(z)} Q_{\text{HII}}(z) \sigma_T \langle n_{\text{H}} \rangle f_{\text{e}}, \quad (15)$$

where c is the speed of light, $H(z)$ the Hubble parameter, Q_{HII} the ionization fraction at redshift z , σ_T the cross-section of electrons to Thomson scattering, $\langle n_{\text{H}} \rangle$ the comoving average number density of hydrogen atoms and f_{e} the fraction of free electrons per hydrogen nucleus in the ionized IGM.

5 IMPLICATIONS FOR COSMIC REIONIZATION

We have shown in Section 3 that introducing non-Gaussianities in the initial density perturbations which are then evolved by means of an N-body code produces measurable effects on the halo mass function, galaxy stellar mass function and far-UV luminosity function. These effects are marginally significant for the non-G 1 and non-G 2 models, while being stronger in the non-G 3 and non-G 4 simulations. This is caused by the different level of non-Gaussianities in the different models, as stronger deviations from purely Gaussian initial conditions produce stronger effects on the quantities considered here. Two general features are shared by all non-Gaussian models considered in this work: the effect of primordial non-Gaussianities on the halo and stellar mass function and on the far-UV luminosity function increases with increasing redshift from $z = 7$ to $z = 14$; this effect becomes stronger at low halo and stellar masses, and thus in faint galaxies (except for the non-G 3 simulation, which show the same level of deviations at low and high masses). This is relevant to the Universe reionization history, since faint galaxies, i.e. galaxies which are currently unobservable

³ Assuming an IGM temperature of $T = 10000$ K would imply a case B recombination coefficient $\alpha_{\text{B}} = 2.59 \times 10^{-13}$, therefore a difference of $\lesssim 3\%$ with respect to our choice.

because of their distance and low luminosity, are thought to be the primary source of ionizing radiation at high redshift.

In this section, we will therefore explore the impact of different levels of primordial non-Gaussianities on the reionization history of the Universe and on the optical depth of electrons to Thomson scattering. This depends on the time-integral of the reionization history, and can be directly measured by CMB observations. We will also show how the emissivity rate of ionizing photons of our models is consistent with recent observations at $2 \lesssim z \lesssim 5$. To explore the effect of different assumptions about the reionization model on our results, we consider three different models, labelled ‘A’, ‘B’ and ‘C’, in which we vary the escape fraction and limiting UV magnitude. Table 3 summarizes our choices for f_{esc} and $M_{\text{FUV}}^{\text{lim}}$ for the three models: model A has $f_{\text{esc}} = 0.2$ at all redshifts and $M_{\text{FUV}}^{\text{lim}} = -12$; model B has the same $M_{\text{FUV}}^{\text{lim}}$ as model A, but f_{esc} that increases with redshift following Equation 11; model C has the same f_{esc} as model B, but a larger $M_{\text{FUV}}^{\text{lim}} = -7$, i.e. it includes fainter galaxies than model A and B. Note that to compute the UV luminosity density for model C (see Equation 12) we adopt a two-piece luminosity function: we consider a Schechter function till $M_{\text{FUV}} = -12$, then a constant function in the range $-12 \leq M_{\text{FUV}} \leq -7$. This is suggested by the recent hydrodynamic simulation of Wise et al. (2014), in which they show that the low efficiency of baryons conversion into stars in low-mass ($\log(M_{\text{halo}}/M_{\odot}) \lesssim 8$) haloes flattens the UV luminosity function at faint luminosities.

5.1 Reionization history of the Universe

We compute the reionization history of the Universe for the different reionization models and both Gaussian and non-Gaussian simulations by numerically integrating Equation 9. For the fixed reionization model, the only quantity that varies in Equation 9 among the Gaussian and non-Gaussian simulations is the production rate of ionizing photons, since it depends on ξ_{ion} , the rate of Lyman-continuum photons per unit UV luminosity, and on ρ_{UV} , the UV galaxy luminosity density. This in turns depends on the far-UV galaxy luminosity function through Equation 12, which we integrate analytically assuming for the parameters of the Schechter function ϕ^* , M^* and α the median of the posterior marginal distributions obtained by an MCMC fitting of the ‘numerical’ luminosity function at each redshift (see Section 3.3).

We show in Fig. 10 the results of the numerical integration of Equation 9, i.e. the fraction of ionized volume of the Universe as a function of redshift. Lines of different colours correspond to the different Gaussian and non-Gaussian simulations; solid lines refer to the reionization model A, dashed lines to model B, and dot-dashed lines to model C.

The solid lines in Fig. 10 indicate that the reionization histories obtained for the Gaussian, non-Gaussian 1, 2 and 3 simulations for the reionization model A show small differences with one another. This is a direct consequence of the similarity of the far-UV luminosity functions among the Gaussian, non-Gaussian 1, 2 and 3 simulations at redshift $z \lesssim 12$, and therefore at most times (see Fig. 8). On the other hand, Fig. 10 shows significant differences among the reionization history of the non-G 4 simulation and the other simulations. At a given redshift, the fraction of the IGM ionized is larger for the non-G 4 simulation, being $Q_{\text{HII}} = 0.08$ (0.53) at redshift $z = 12$ (8), to be compared with $Q_{\text{HII}} \sim 0.04$ (0.45) at the same redshifts for the other simulations. This difference is a direct consequence of the larger number of low-mass galaxies formed in the non-G 4 simulation with respect to the other simulations (see

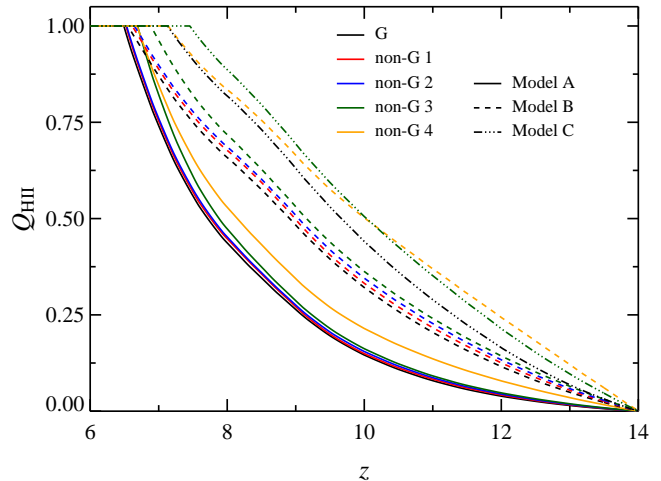


Figure 10. Ionization fraction of the Universe as a function of redshift obtained by applying the different reionization models of Table 3 to the different Gaussian and non-Gaussian simulations. Different colours indicate different simulations: Gaussian (black), non-Gaussian 1 (red), non-Gaussian 2 (blue), non-Gaussian 3 (dark green) and non-Gaussian 4 (orange). Solid lines refer to the reionization model A ($f_{\text{esc}} = 0.2$ and $M_{\text{FUV}}^{\text{lim}} = -12$), dashed lines to model B (f_{esc} increasing with z as in Equation (11) and $M_{\text{FUV}}^{\text{lim}} = -12$), dot-dashed lines to model C (f_{esc} increasing with z as in Equation (11) and $M_{\text{FUV}}^{\text{lim}} = -7$). For clarity, for this latter model we just plot the results for the Gaussian and non-Gaussian 3 simulations.

Fig. 8(d)), which, at each redshift, increases the number of photons available for hydrogen ionization.

The dashed lines in Fig. 10 show the reionization histories for the different simulations obtained assuming the reionization model B, which, unlike model A, has an escape fraction that increases with increasing redshift. This makes the fraction of ionized IGM to increase more rapidly at high z , because of the larger number of photons available for hydrogen ionization at high redshift in model B than in model A. As for model A, the reionization histories of the Gaussian simulation and non-Gaussian simulation 1, 2 and 3 show smaller differences than that of the non-G 4 simulation. We note, however, that the dashed lines in Fig. 10 are more separated than the solid ones, indicating that a model with an escape fraction that increases with redshift boosts the effect of primordial non-Gaussianities on the Universe reionization history. The reason is that in such a model the ionizing radiation emitted by higher redshift galaxies can escape the ISM more easily, hence increasing the contribution to Universe reionization of galaxies at high z , those most affected by primordial non-Gaussianities.

In Fig. 10, we show as dot-dashed lines Q_{HII} for model C, which has a higher (fainter) $M_{\text{FUV}}^{\text{lim}}$ than models A and B. For clarity, we just plot Q_{HII} for the Gaussian and non-Gaussian 3 simulations. Fig. 10 shows that considering fainter galaxies than those considered in models A and B makes Q_{HII} increase faster at $z \gtrsim 10$, while at same time increasing the difference between the Gaussian and non-Gaussian model 3. The explanation is similar to that given above for model B, but it appeals to the increasing effect of non-Gaussianities with decreasing galaxy luminosity, as adopting higher values of $M_{\text{FUV}}^{\text{lim}}$ increases the weight of very faint galaxies, those most affected by non-Gaussianities, towards reionization.

5.2 Electron Thomson scattering optical depth

Direct measurements of the Universe ionized fraction through Ly α absorption from background quasars are effective up to neutral fractions $(1 - Q_{\text{HII}}) \sim 10^{-3}$, since at higher values of $(1 - Q_{\text{HII}})$ the resonance introduced by Ly α scattering makes ionizing photons almost completely absorbed by neutral hydrogen the IGM. This situation may change in the future through measurements of the 21 cm emission from the hyper-fine transition of neutral hydrogen, since this quantity directly depends on the hydrogen reionization history (e.g. see the review of Morales & Wyithe 2010). For now, one of the most important constraints on cosmic reionization comes from the optical depth of electrons to Thomson scattering τ_e , since this quantity depends on the (integrated) ionization fraction at different redshifts (see Equation (15)) and can be measured through CMB photons.

We show in Fig. 11 the optical depth of electrons to Thomson scattering for the different reionization models, for the Gaussian and non-Gaussian simulations, obtained by numerically integrating Equation 15. As in Fig. 10, different colours refer to different simulations, solid lines to the reionization model A, dashed lines to model B, and dot-dashed lines to model C.

As for the reionization history shown in Fig. 10, solid lines in Fig. 11 indicate that the values of τ_e obtained from the Gaussian and non-Gaussian simulation 1, 2 and 3 show small differences when assuming a reionization model with constant escape fraction. As in Fig. 10, the non-G 4 simulation produces the largest difference in this quantity. This is not surprising, since the only term which varies in the computation of the electron optical depth is the fraction ionized at each redshift (see Equation (15)), which shows large variations between the non-G 4 simulation and the other simulations. Fig. 10 shows also that assuming a constant escape fraction $f_{\text{esc}} = 0.2$ produces an optical depth τ_e lower than the values currently allowed by *Planck* observations, for all models. This suggests that a higher escape fraction and/or a fainter limiting UV magnitude are required to reionize earlier the Universe and obtain τ_e in agreement with *Planck* constraints.

The dashed lines in Fig. 11 show τ_e for model B, in which the escape fraction increases with increasing redshift. Unlike model A, this one produces values of τ_e within the *Planck* constraints for all Gaussian and non-Gaussian simulations. As we have already highlighted for the reionization history, this model boosts the effect of primordial non-Gaussianities, increasing the differences in the Thomson scattering optical depth among all simulations. This is a direct consequence of the different reionization histories, and of the increased ‘weight’ that an increasing f_{esc} with redshift gives to high redshift galaxies, those most affected by primordial non-Gaussianities.

The dot-dashed lines in Fig. 11 show the effect of increasing the limiting UV magnitude from -12 to -7 for the Gaussian and non-Gaussian 3 simulations. This increases, at a given redshift, the value of τ_e with respect to models A and B, while at the same time boosting the differences between the G and non-G 3 models. As we already noted for Q_{HII} , the cause is the increased weight of very faint galaxies to reionization, that is of the galaxies most affected by non-Gaussianities.

5.3 Ionizing emissivity

We have shown in Fig. 11 that our models with variable escape fraction (models B and C) predict values of τ_e within *Planck* con-

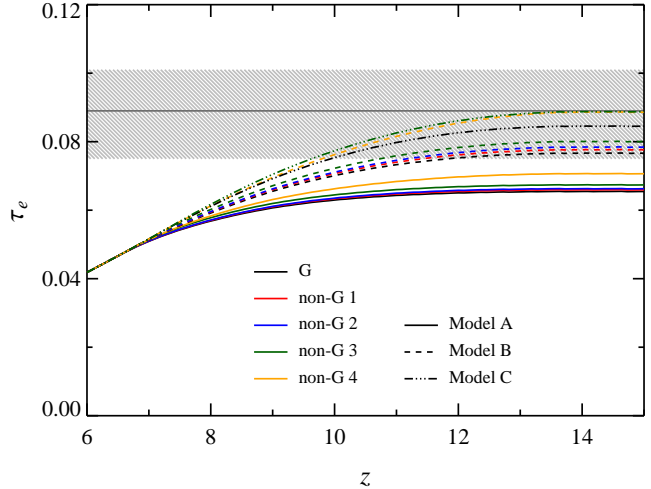


Figure 11. Optical depth of electrons to Thomson scattering as a function of redshift obtained by numerically integrating Equation (15). The dark-grey solid line indicates the ‘best-fit’ value of τ_e along with the 68 % confidence limits (grey hatched region), obtained by Planck Collaboration (2014) (see their Table 5, first column). Lines of different colours refer to different simulations: Gaussian (black), non-Gaussian 1 (red), non-Gaussian 2 (blue), non-Gaussian 3 (dark green) and non-Gaussian 4 (orange). Solid lines refer to the reionization model A ($f_{\text{esc}} = 0.2$ and $M_{\text{FUV}}^{\text{lim}} = -12$), dashed lines to model B (f_{esc} increasing with z as in Equation (11) and $M_{\text{FUV}}^{\text{lim}} = -12$), dot-dashed lines to model C (f_{esc} increasing with z as in Equation (11) and $M_{\text{FUV}}^{\text{lim}} = -7$). For clarity, for this latter model we just plot the results for the Gaussian and non-Gaussian 3 simulations.

straints. However, this does not guarantee our models to be consistent with the (comoving) ionizing emissivity rate measured from the IGM opacity to Ly α photons. We therefore compute the ionizing emissivity rate of our reionization models, for the Gaussian and non-Gaussian simulations, and compare our results with the measures by Becker & Bolton (2013) of the ionizing emissivity at $2 \leq z \leq 5$. Note that in order to compare our predictions with the Becker & Bolton (2013) data, we have to extrapolate the predicted far-UV luminosity function to lower redshift, as our simulations stop at $z = 6.5$. We therefore consider the relations between the free parameters of the Schechter function (ϕ^* , M^* and α) and redshift, and note that these relations are linear in the range $6.5 \leq z \leq 9$. We therefore adopt a linear extrapolation to compute the far-UV luminosity function and ionizing emissivity rate down to $z = 5$.

We show in Fig. 12 as shaded areas the emissivities predicted by the reionization models A (dark grey), B (grey), and C (black), while we indicate with black circles Becker & Bolton (2013) data. The width of the shaded areas at each redshift reflects the range of emissivities of the different Gaussian and non-Gaussian simulations. Fig. 12 shows that at high redshift our reionization models span a wide range of ionizing emissivities, while at $z = 5$ the predictions of all models agree with Becker & Bolton (2013) observations. Fig. 12 also shows that the relative emissivities of models A, B and C are mainly driven by the adopted relation between escape fraction and redshift: at $z \gtrsim 8$ the escape fraction is larger in models B and C than in model A, and so is the emissivity, while at $z \lesssim 7$ the situation is reversed, as the escape fraction of model A becomes larger than that of models B and C.

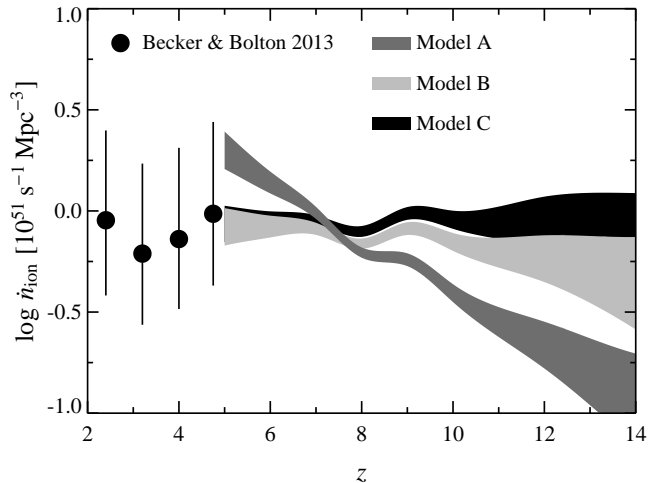


Figure 12. Ionizing emissivity as a function of redshift for the different reionization models adopted in this work. Black circles indicate the ionizing emissivity measured by Becker & Bolton (2013) at $2 \leq z \leq 5$. The shaded regions refer to different reionization models: model A (dark grey shaded region, $f_{\text{esc}} = 0.2$ and $M_{\text{FUV}}^{\text{lim}} = -12$), model B (grey shaded region, f_{esc} increasing with z as in Equation (11) and $M_{\text{FUV}}^{\text{lim}} = -12$); model C (black shaded region, f_{esc} increasing with z as in Equation (11) and $M_{\text{FUV}}^{\text{lim}} = -7$). Note that the width of each shaded region reflects, for the fixed reionization model, the range spanned by the different Gaussian and non-Gaussian simulations, without accounting for other sources of errors (e.g. uncertainties in the luminosity function fit with a Schechter function, uncertainties in the free parameters of the reionization model).

6 UNCERTAINTIES IN THE REIONIZATION MODEL

The model of cosmological reionization that we have adopted depends on several assumptions, which we will discuss in this section. We firstly address our choice of neglecting the contribution of AGN and Pop III stars to cosmological reionization. Then, we discuss our assumptions about the adjustable parameters of the reionization model, namely the escape fraction, limiting UV magnitude and clumping factor. Finally, we justify our choice of not including dust attenuation in our model.

6.1 Contribution of Active Galactic Nuclei and Pop III to hydrogen reionization

In our model of cosmic reionization we have ignored the contribution of active galactic nuclei (AGN) and Pop III stars to the hydrogen ionizing budget; within our model the only sources of ionizing radiations are metal-enriched stars residing in galaxies.

AGN do not contribute significantly to hydrogen reionization because their number density rapidly decreases at $z \gtrsim 3$ (e.g. Hopkins et al. 2007; Ross et al. 2013), and therefore they add few UV photons to those produced by massive stars (e.g. Faucher-Giguère et al. 2009). Nevertheless, Volonteri & Gnedin (2009) have pointed out that secondary ionization from X-ray emission could boost AGN contribution to reionization up to 50-90 % at $z \gtrsim 8$. However, Grissom et al. (2014) have recently re-addressed this question, reaching a different conclusion. They consider the most recent constraints on the AGN X-ray luminosity function, and adopt a conservative model in which AGN accrete at the maximum (Eddington) rate and are unobscured. They consider primary and secondary ionization from X-ray photons, and find that the AGN

contribution to Universe reionization is $\lesssim 14\%$ at all redshifts $6 \leq z \leq 14$ (see their figure 3).

Metal-free ‘Pop III’ stars form from pristine gas which has not yet been enriched by previous generation of stars. The absence of metals and dust grains suggest that fragmentation of molecular clouds is less efficient, and simulations have indeed shown that the first stars form with an initial mass function richer in high mass stars than what observed in the Local Universe (e.g. McKee & Tan 2008; Clark et al. 2011), even though no observational constraints on their masses currently exist. Pop III stars are therefore thought to be massive and short-lived, and, despite their hot temperatures and hard-radiation spectrum, to give little contribution to the total budget of hydrogen ionizing photons (e.g. see figure 12 of Wise et al. 2014 and figure 2 of Paardekooper et al. 2013). We note also that the chemical abundances of the IGM measured from damped Ly α systems at $z \lesssim 6$ suggests a low contribution of Pop III stars to Universe reionization, as the yields of massive Pop III stars would leave peculiar imprints, which are not observed, on these abundances (e.g. Becker et al. 2012; Kulkarni et al. 2014).

6.2 Effect of changes in the adjustable parameters of the reionization model

The reionization model we have presented in Section 4 depends on three adjustable parameters: the escape fraction of ionizing photons, limiting UV magnitude and clumping factor. These parameters are poorly constrained at high redshift by current observations, and therefore they are the major sources of uncertainty in modelling cosmological reionization. In this section, we discuss our choices for these three adjustable parameters, and how their variation will affect our results.

6.2.1 Escape fraction

The fraction of ionizing (Lyman-continuum) photons escaping the ISM of the galaxies in which they are produced alters the amount of photons available for hydrogen ionization, therefore affecting the reionization history of the Universe (see Equations 9 and 10). Observations can accurately constrain f_{esc} only in the local Universe, e.g. the (angle-averaged) Milky Way escape fraction is $\langle f_{\text{esc}} \rangle \sim 0.02$ (Bland-Hawthorn & Maloney 1999). Adopting such a low value for the escape fraction would make Universe reionization by star-forming galaxies alone very challenging. At higher redshift constraints on f_{esc} are more uncertain, however data suggest that the escape fraction at $z \sim 3$ is $\sim 0.05 - 0.07$ for Lyman-break galaxies (LBG), and $\sim 0.1 - 0.3$ for (fainter) Lyman-alpha emitters (LAE) (Nestor et al. 2013, see also Jones et al. 2013), pointing toward an increase of the escape fraction with increasing redshift.

Local constraints on f_{esc} are of limited use at high redshift, since the escape fraction depends, among other parameters, on galaxy morphologies, stellar feedback, and more in general on the interplay between galaxies and the IGM, while the available observational constraints at high redshift are still very uncertain. This has motivated in the last few years the development of extensive simulations to study how the escape fraction varies in dwarf galaxies at high redshift.

Different groups have found consistent trends in their sophisticated hydrodynamical simulations of star-bursting dwarf galaxies (Wise & Cen 2009; Paardekooper et al. 2013; Wise et al. 2014; So et al. 2014; Kimm & Cen 2014). They find f_{esc} in these high redshift dwarf galaxies to be higher than in local disk galaxies

($f_{\text{esc}} > 0.1$ for high- z dwarf), and to be tightly correlated to their star formation rate. Moreover, they find systematically larger escape fractions with decreasing halo mass. They explain these trends as follows: the irregular morphology of high- z dwarf galaxies boosts f_{esc} with respect to local discs since star formation is not confined along the equatorial disc of the galaxies, hence UV radiation escaping star forming regions is less likely to be absorbed during its travel along the disc. Dwarf galaxies are also more affected by stellar feedback (i.e. ionization fronts, winds, shocks from supernovae) because of their shallower potential wells and irregular morphology. This also explains the trend they observe with halo mass, as feedback in lower mass haloes is more efficient in removing gas and creating cavities along which the ionizing radiation can escape. The dependence of f_{esc} on the star formation rate is also caused by stellar feedback, as a burst of star formation clears out the gas from the galaxy, allowing photons to escape more easily and increasing f_{esc} .

To summarize, hydrodynamical simulations from different groups consistently show that the escape fraction is larger in high- z dwarf galaxies than in low- z discs; f_{esc} in high- z galaxies is time- and space-dependent since it depends on the interplay between stellar feedback and gas in the ISM; f_{esc} increases with decreasing halo mass. Our choice of a constant escape fraction $f_{\text{esc}} = 0.2$ at all halo masses and redshift is therefore conservative, while our model with f_{esc} increasing with redshift is based upon the above results, since, as the average halo mass decreases with increasing redshift, we expect the escape fraction to increase. This, as shown by the dashed lines in Figs. 10–11, increases the effect of primordial non-Gaussianities on the Universe reionization history, since a larger fraction of the photons emitted by high redshift ($z \gtrsim 10$) galaxies, those most affected by primordial non-Gaussianities, becomes available for hydrogen ionization.

6.2.2 Limiting UV magnitude

The limiting UV magnitude affects the UV luminosity density (via the integral of Equation 12), and therefore the reionization history of the Universe (see Equations 9 and 10). This quantity depends on the minimum mass of a halo able to cool down the gas and sustain star formation. Constraining this quantity with data requires observing the faintest galaxies at high redshift, a task which will be very difficult even with the next generation of telescopes such as *JWST* (e.g. see fig 15 of Wise et al. 2014). This means that, as for the escape fraction, we have to rely on simulations to constrain the limiting UV magnitude.

For a long time, it has been thought that only haloes hosting atomic hydrogen (i.e. with $T_{\text{vir}} > 10^4$ K, or $\log(M_{\text{halo}}/M_{\odot}) \gtrsim 8$) can cool gas down to the temperatures required for stars to form (e.g. Bromm & Loeb 2003). The reason is that earlier models over-predicted the efficiency of UV background (Lyman-Werner) radiation in dissociating hydrogen molecules, hence preventing them from being an effective gas coolant. In the past few years, however, several groups (e.g. Wise & Abel 2007; O’Shea & Norman 2008) have shown by means of sophisticated hydrodynamical simulations that hydrogen molecules can survive even in the presence of an extreme UV background, and that they can therefore act as an effective coolant in haloes with masses $\log(M_{\text{halo}}/M_{\odot}) \lesssim 8$. In particular, Wise et al. (2014) show that haloes with masses as low as $\log(M_{\text{halo}}/M_{\odot}) \sim 6.5$, corresponding to $M_{\text{FUV}} \sim 5.5$, can host dense molecular gas able to form stars. The same authors find however an almost constant number density of faint galaxies

($M_{\text{FUV}} \gtrsim -12$), unlike what one would expect by extrapolating the galaxy luminosity function to very faint luminosities.

In our model, we have chosen a limiting UV magnitude $M_{\text{FUV}}^{\text{lim}} = -12$, similar to what has been assumed in previous works (e.g. Robertson et al. 2013) and in agreement with the Wise et al. (2014) predictions for an extrapolation of the luminosity function at faint magnitudes. We have also explored that the effect of increasing $M_{\text{FUV}}^{\text{lim}}$ on the Universe reionization history: assuming $M_{\text{FUV}}^{\text{lim}} > -12$ increases the ‘weight’ of low-mass galaxies to the reionization budget, thus boosting the effect of non-Gaussianities in a qualitatively similar way to what we observed for the escape fraction (see Fig. 11). On the other hand, considering $M_{\text{FUV}}^{\text{lim}} < -12$ would reduce the effect primordial non-Gaussianities on cosmological reionization, although in this case, other sources of ionizing radiation would be required to match *Planck* constraints on τ_e .

6.2.3 Clumping factor

The clumping factor accounts for inhomogeneities in the density, temperature and ionization fields of the IGM. These inhomogeneities make the recombination rate computed assuming a density and temperature averaged over the whole Universe different from that computed from averaging over HII regions, since this rate depends on the local temperature and density of electrons and protons. A clumping factor $C_{\text{HII}} > 1$ reduces the recombination time (see Equation 13), delaying reionization with respect to a case in which $C_{\text{HII}} \leq 1$. As for the escape fraction and limiting UV magnitude, the clumping factor too can only be studied only through simulations, since there are no observations of this quantity at the redshifts of interest for reionization.

A common definition of the clumping factor in simulations involves only the gas density $C_{\text{HII}} = \langle \rho^2 \rangle_{\text{IGM}} / \langle \rho \rangle^2$, where ρ indicates the baryon density and brackets refer to a volume-average over the recombining IGM and over the whole Universe. By adopting such a definition, early simulations obtained large clumping factors $C_{\text{HII}} \sim 30$ (e.g. Gnedin & Ostriker 1997), which would make reionization hard to achieve with star-forming galaxies alone. More recent works consider a density threshold in order to separate gas in the ISM from gas in the IGM, accounting also for photo-ionization by a UV background. This lowers the clumping factor by almost an order of magnitude ($C_{\text{HII}} \sim 3$ at $z = 6$), and predicts a decreasing C_{HII} with increasing redshift (Pawlik et al. 2009). However, a limitation of the model of Pawlik et al. (2009) is that it assumes an optically thin IGM, therefore not accounting for self-shielding in over-dense regions.

This limitation has been overcome in the recent simulation of Finlator et al. (2012), in which they include a sub-grid model for the self-shielding of over-dense regions in the IGM. They find that the density threshold for self-shielding evolves with redshift, as it depends on both the UV background and gas temperature, which in turns varies with z . Their main result is that accounting for both self-shielding and fluctuations in the IGM temperature further reduces the clumping factor with respect to Pawlik et al. (2009) values (see figure 3 of Finlator et al. 2012). We therefore adopt equation 8 of Finlator et al. (2012), which is valid in the redshift range $5 \leq z \leq 15$, to describe the evolution with redshift of the clumping factor in our reionization model. This equation predicts a clumping factor which decreases with increasing redshift (see figure 11 of Wise et al. 2014 for a similar prediction), i.e. a larger recombination time at high redshift with respect to a model in which C_{HII} is constant with redshift (e.g. as in Robertson et al. 2013). Similarly to the effect of an escape fraction that increases with redshift,

this boosts the effect of primordial non-Gaussianities on cosmological reionization, since a lower clumping factor at high redshift increases the recombination time (see Equations 9 and 13), hence enhancing the efficiency of high ($z \gtrsim 10$) galaxies, those most affected by non-Gaussianities, in ionizing hydrogen.

6.3 Dust attenuation

Simulations have shown that dust in high- z galaxies has little effect on f_{esc} , as the absorption cross section of Lyman-continuum photons to dust is much smaller than to neutral hydrogen (e.g. Gnedin et al. 2008; Paardekooper et al. 2011). We have also neglected dust attenuation when matching our predictions for the far-UV luminosity function with the Bouwens et al. (2014) observations at $z = 7$ and 8. This is supported by the recent work of Wilkins et al. (2013), who consider the UV continuum slope of a large sample of star-forming galaxies at $z \gtrsim 5$. They estimate the amount of UV attenuation affecting their sample by considering different attenuation and extinction curves, so as to minimise the model-dependence of their results. They find that UV attenuation decreases with increasing redshift, at fixed UV luminosity, so that at $z \sim 6$ the mean far-UV attenuation of galaxies with $M_{\text{FUV}} \sim -21.5$ is in the range 0.5 – 1.5, decreasing to 0.5 – 1 at $z = 7$, with the exact values depending on the adopted curve. They also find that A_{FUV} decreases with decreasing UV luminosity, at fixed redshift, so that at $z = 7$ the far-UV attenuation is in the range 0 – 0.5 for galaxies with $M_{\text{FUV}} \lesssim -20.3$. This suggests that dust corrections are not important for most galaxy luminosities and redshifts considered in this work.

7 CONCLUSIONS

Understanding the details of cosmological reionization is one of the big challenges of current high redshift astronomy. Observations have established that at high redshift ($z \gtrsim 6$), low-mass galaxies outnumbered high-mass galaxies more than at lower redshift, i.e. that the UV luminosity function becomes steeper with increasing redshift (e.g. Bouwens et al. 2014). This, combined with the observed decline of the AGN number density at $z \gtrsim 3$ and the predicted negligible contribution to the ionizing budget of Pop III stars, suggests that dwarf galaxies at $z \gtrsim 6$ are likely responsible for cosmological reionization.

In this work, we have extended the analysis of paper I on the impact of scale-dependent non-Gaussianities by considering their effects on the UV galaxy luminosity function and on the reionization history of the Universe. Specifically, we have run 5 cosmological N-body simulations with identical power spectra, but different scale-dependent primordial non-Gaussianities, all consistent with *Planck* constraints. As in paper I, we have shown that models with stronger initial non-Gaussianities produce larger effects (up to a factor of 3) on the halo mass function, and that this effect increases with increasing redshift, at fixed halo mass. We find in all simulations except the one with the steepest scale-dependent non-Gaussianity that the effect of such primordial non-Gaussianities is more significant in low- than high-mass haloes, at fixed redshift.

By combining the halo merger trees obtained from simulations with different initial conditions together with a modified version of the galaxy formation model of Mutch et al. (2013) and the Bruzual & Charlot (2003) population synthesis code, we have then matched the most recent determination of the far-UV galaxy luminosity function at $z = 7$ and 8. We have also shown that the pre-

diction of our model for the evolution of the faint-end slope of the far-UV galaxy luminosity function is in excellent agreement with observations at $z = 6 - 10$. This demonstrates that a phenomenological galaxy formation model which subsumes the complex baryonic physics in a few analytic functions is accurate enough to predict the observed properties of the galaxy population at high redshift.

Having calibrated in such a way the galaxy formation model, we apply it to the different simulations with non-Gaussian initial conditions, showing that the effects introduced by non-Gaussianities on the distribution of halo masses propagate to the galaxy stellar mass function and far-UV luminosity function. In particular, the initial non-Gaussianities considered in this work increase the number density of faint galaxies (up to a factor of 3), and this effect becomes stronger with increasing redshift, at fixed UV magnitude and similarly to what noted for the halo mass function.

Finally, we have appealed to an analytic reionization model to quantify the effect of primordial non-Gaussianities on the reionization history of the Universe. We find that the effect of such non-Gaussianities depends on the adopted reionization model, and in particular on the adopted values for the ionizing escape fraction and limiting UV magnitude. For a given set of parameters describing the far-UV luminosity function, these two quantities, along with the clumping factor, determine the relative contribution to Universe reionization of galaxies at different redshifts, and hence the impact of primordial non-Gaussianities, as their effect is strongly redshift-dependent.

We find that adopting a (redshift-dependent) ionizing escape fraction and clumping factor, as predicted by state-of-the-art hydrodynamical simulations, boosts the imprint of primordial non-Gaussianities on the reionization history of the Universe and on the electron Thomson scattering optical depth. The same qualitative effect is produced by decreasing the limiting UV luminosity, i.e. by considering stars residing in ‘mini-haloes’ (down to $\log(M_{\text{halo}}/M_{\odot}) \sim 6$, as in Wise et al. 2014). We also find that our reionization models with ionizing escape fraction increasing with redshift produce τ_e in agreement with *Planck* constraints, while at the same time allowing us to match the ionizing emissivity rate measured at $z \sim 5$. Although current uncertainties on the physics of reionization and on the determination of τ_e dominate the signal of non-Gaussianities, more accurate measurements of this quantity, combined to a better understanding of the ingredients of reionization models, have the potential to constrain the shape of primordial density fluctuations, and may eventually be used to narrow down the allowed model-space of inflation.

ACKNOWLEDGMENTS

We thank the anonymous referee for insightful comments which helped improving the paper. We are grateful to Kristian Finlator and Stephane Charlot for their comments on an early draft of this paper, which helped us improving the work. JC acknowledges the support of the European Research Council via Advanced Grant N° 267117 (DARK, P.I. Joseph Silk) and via Advanced Grant N° 321323 (NEOGAL, P.I. Stephane Charlot). TN is supported by the Japan Society for the Promotion of Science (JSPS) Postdoctoral Fellowships for Research Abroad.

References

Alishahiha M., Silverstein E., Tong D., 2004, Phys. Rev. D, 70,

- 123505
 Alvarez M. A., Finlator K., Trenti M., 2012, *ApJ*, 759, L38
 Aubert D., Pichon C., Colombi S., 2004, *MNRAS*, 352, 376
 Becker A., Huterer D., Kadota K., 2011, *JCAP*, 1, 6
 Becker G. D., Bolton J. S., 2013, *MNRAS*, 436, 1023
 Becker G. D., Sargent W. L. W., Rauch M., Carswell R. F., 2012, *ApJ*, 744, 91
 Behroozi P. S., Wechsler R. H., Conroy C., 2013, *ApJ*, 770, 57
 Berlind A. A., Weinberg D. H., 2002, *ApJ*, 575, 587
 Berlind A. A. et al., 2003, *ApJ*, 593, 1
 Bland-Hawthorn J., Maloney P. R., 1999, *ApJ*, 510, L33
 Bouwens R. J. et al., 2014, *ArXiv e-prints*
 Bromm V., Loeb A., 2003, *ApJ*, 596, 34
 Bruzual G., Charlot S., 2003, *MNRAS*, 344, 1000
 Cen R., Ostriker J. P., 2006, *ApJ*, 650, 560
 Chabrier G., 2003, *PASP*, 115, 763
 Chen X., 2005, *Phys. Rev. D*, 72, 123518
 Clark P. C., Glover S. C. O., Klessen R. S., Bromm V., 2011, *ApJ*, 727, 110
 Coc A., Uzan J.-P., Vangioni E., 2013, *ArXiv e-prints*
 Cole S., Lacey C. G., Baugh C. M., Frenk C. S., 2000, *MNRAS*, 319, 168
 Conroy C., Wechsler R. H., Kravtsov A. V., 2006, *ApJ*, 647, 201
 Crocce M., Pueblas S., Scoccimarro R., 2006, *MNRAS*, 373, 369
 Crociani D., Moscardini L., Viel M., Matarrese S., 2009, *MNRAS*, 394, 133
 Croton D. J. et al., 2006, *MNRAS*, 365, 11
 Fan X., Carilli C. L., Keating B., 2006, *ARA&A*, 44, 415
 Faucher-Giguère C.-A., Lidz A., Zaldarriaga M., Hernquist L., 2009, *ApJ*, 703, 1416
 Finlator K., Oh S. P., Özel F., Davé R., 2012, *MNRAS*, 427, 2464
 Fukugita M., Hogan C. J., Peebles P. J. E., 1998, *ApJ*, 503, 518
 Gnedin N. Y., Kravtsov A. V., Chen H.-W., 2008, *ApJ*, 672, 765
 Gnedin N. Y., Ostriker J. P., 1997, *ApJ*, 486, 581
 Grissom R. L., Ballantyne D. R., Wise J. H., 2014, *A&A*, 561, A90
 Habouzit M., Nishimichi T., Peirani S., Mamon G. A., Silk J., Chevallard J., 2014, *ArXiv e-prints*
 Henriques B. M. B., White S. D. M., Thomas P. A., Angulo R. E., Guo Q., Lemson G., Springel V., 2013, *MNRAS*, 431, 3373
 Hopkins P. F., Richards G. T., Hernquist L., 2007, *ApJ*, 654, 731
 Jones T. A., Ellis R. S., Schenker M. A., Stark D. P., 2013, *ApJ*, 779, 52
 Kauffmann G., White S. D. M., Guiderdoni B., 1993, *MNRAS*, 264, 201
 Kimm T., Cen R., 2014, *ApJ*, 788, 121
 Kirby E. N., Cohen J. G., Guhathakurta P., Cheng L., Bullock J. S., Gallazzi A., 2013, *ApJ*, 779, 102
 Komatsu E., Spergel D. N., 2001, *Phys. Rev.*, D63, 063002
 Kuhlen M., Faucher-Giguère C.-A., 2012, *MNRAS*, 423, 862
 Kulkarni G., Hennawi J. F., Rollinde E., Vangioni E., 2014, *ApJ*, 787, 64
 Lo Verde M., Miller A., Shandera S., Verde L., 2008, *JCAP*, 4, 14
 Lu Y., Mo H. J., Weinberg M. D., Katz N., 2011, *MNRAS*, 416, 1949
 Madau P., Haardt F., Rees M. J., 1999, *ApJ*, 514, 648
 Matarrese S., Verde L., Jimenez R., 2000, *ApJ*, 541, 10
 McKee C. F., Tan J. C., 2008, *ApJ*, 681, 771
 Morales M. F., Wyithe J. S. B., 2010, *ARA&A*, 48, 127
 Moster B. P., Naab T., White S. D. M., 2013, *MNRAS*, 428, 3121
 Mutch S. J., Croton D. J., Poole G. B., 2013, *MNRAS*, 435, 2445
 Nestor D. B., Shapley A. E., Kornei K. A., Steidel C. C., Siana B., 2013, *ApJ*, 765, 47
 Nishimichi T., 2012, *JCAP*, 8, 37
 Nishimichi T. et al., 2009, *PASJ*, 61, 321
 Nishimichi T., Taruya A., Koyama K., Sabiu C., 2010, *JCAP*, 7, 2
 Oesch P. A. et al., 2013, *ApJ*, 773, 75
 O'Shea B. W., Norman M. L., 2008, *ApJ*, 673, 14
 Paardekooper J.-P., Khochfar S., Dalla Vecchia C., 2013, *MNRAS*, 429, L94
 Paardekooper J.-P., Pelupessy F. I., Altay G., Kruij C. J. H., 2011, *A&A*, 530, A87
 Pawlik A. H., Schaye J., van Scherpenzeel E., 2009, *MNRAS*, 394, 1812
 Planck Collaboration, 2014, *A&A*, 566, A54
 Planck Collaboration et al., 2013, *ArXiv e-prints*
 Robertson B. E. et al., 2013, *ApJ*, 768, 71
 Ross N. P. et al., 2013, *ApJ*, 773, 14
 Schechter P., 1976, *ApJ*, 203, 297
 Scoccimarro R., 1998, *MNRAS*, 299, 1097
 Shandera S., Dalal N., Huterer D., 2011, *JCAP*, 3, 17
 Silverstein E., Tong D., 2004, *Phys. Rev. D*, 70, 103505
 So G. C., Norman M. L., Reynolds D. R., Wise J. H., 2014, *ApJ*, 789, 149
 Springel V., 2005, *MNRAS*, 364, 1105
 Springel V., Yoshida N., White S. D. M., 2001, *New Astronomy*, 6, 79
 Tacchella S., Trenti M., Carollo C. M., 2013, *ApJ*, 768, L37
 Tweed D., Devriendt J., Blaizot J., Colombi S., Slyz A., 2009, *A&A*, 506, 647
 Valageas P., Nishimichi T., 2011, *A&A*, 527, A87
 Volonteri M., Gnedin N. Y., 2009, *ApJ*, 703, 2113
 Wilkins S. M., Bunker A., Coulton W., Croft R., Matteo T. D., Khandai N., Feng Y., 2013, *MNRAS*, 430, 2885
 Wise J. H., Abel T., 2007, *ApJ*, 671, 1559
 Wise J. H., Cen R., 2009, *ApJ*, 693, 984
 Wise J. H., Demchenko V. G., Halicek M. T., Norman M. L., Turk M. J., Abel T., Smith B. D., 2014, *ArXiv e-prints*
 Yadav A. P. S., Wandelt B. D., 2010, *Advances in Astronomy*, 2010
 Zheng Z. et al., 2005, *ApJ*, 633, 791